CANCER

In vivo generation of CAR myeloid cells through erythrocyte-mediated mRNA delivery for cancer immunotherapy

Xiaoqian Nie[1,2]†, Yuehua Liu[1,2,3]†, Yuting Song[4]†, Xingyun Yao[1,2]†, Yangyang Chen[4], Hsiang-Ying Lee[5,6]*, Xiaofei Gao[1,2,3]*

Engineering myeloid cells with chimeric antigen receptors (CARs) holds great therapeutic promise, but their generation in vivo remains challenging. Here, we developed an erythrocyte-mediated messenger RNA (mRNA) delivery platform, termed mRNA-LNP-Ery, in which mRNA-loaded lipid nanoparticles (LNPs) are covalently anchored onto erythrocytes. Exploiting erythrocytes' intrinsic splenic homing capacity and unique biocompatibility, mRNA-LNP-Ery enables highly selective and efficient mRNA delivery to CD11b$^+$ myeloid cells in the spleen, with minimal uptake by hepatocytes. We also demonstrated that mRNA-LNP-Ery is internalized through phagocytosis and avoids lysosomal degradation, resulting in enhanced cytosolic mRNA translation. Delivery of mRNAs encoding CARs targeting human epidermal growth factor receptor 2 (HER2) or CD19 generated functional CAR myeloid cells in vivo that adopted a proinflammatory, antigen-presenting phenotype. These cells migrated to tumors, eliminated cancer cells, and remodeled the tumor microenvironment, leading to increased infiltration of effector T and natural killer (NK) cells. The antitumor effect was abolished in splenectomized mice and partially diminished in nude mice, indicating that therapeutic activity depends on both CAR myeloid cell formation within the spleen and their cross-talk with adaptive immunity. Furthermore, repeated administration of mRNA-LNP-Ery achieved superior antitumor efficacy to conventional mRNA-LNPs at one-tenth the mRNA dose, with minimal systemic toxicity, underscoring the high efficiency and safety of spleen-targeted delivery. Together, our findings established a clinically translatable erythrocyte-based mRNA platform that enables direct in vivo immune cell programming and advances CAR myeloid therapies for solid tumors.

INTRODUCTION

Engineering myeloid cells to express chimeric antigen receptors (CARs) has recently emerged as a promising strategy in cancer immunotherapy, enabling targeted tumor cell phagocytosis and activation of innate and adaptive antitumor immunity (*1*, *2*). Although ex vivo–generated CAR myeloid therapies have shown potential in both preclinical and clinical studies, their clinical translation remains limited by inefficient genetic modification, suboptimal functional durability, and complex manufacturing requirements (*3*). Recent advancements in lipid nanoparticle (LNP)–based mRNA delivery, exemplified by the successful severe acute respiratory syndrome coronavirus 2 (SARS-CoV-2) mRNA vaccines (*4*, *5*), have demonstrated considerable potential for the in vivo genetic engineering of immune cells (*6*). Nevertheless, systemic administration of LNPs remains constrained by biological barriers, including predominant hepatic sequestration through apolipoprotein E (ApoE)–mediated uptake (*7*), vascular endothelial barriers, rapid clearance by the mononuclear phagocyte system (*8*), poor endosomal escape efficiency (*9*), and off-target toxicity (*10*). Collectively, these limitations restrict the efficacy and clinical applicability of conventional LNP-mediated CAR myeloid cell generation in vivo.

The spleen, the largest secondary lymphoid organ in mammals, harbors substantial immune cell populations and serves as the primary reservoir for myeloid cells, making it an attractive target for in vivo immune cell engineering (*11*, *12*). Although recent efforts have used modified LNP formulations to improve selective mRNA delivery to splenic immune cells, these approaches frequently compromise nanoparticle stability, alter surface charges, and ultimately decrease mRNA expression efficiency (*13*, *14*). Moreover, the spleen's unique anatomical structure and stringent immune surveillance mechanisms further impede efficient nanoparticle-mediated delivery (*15*, *16*). In contrast, erythrocytes naturally pass through the spleen ~70 times daily, undergoing routine surveillance by splenic myeloid cells responsible for clearing aged or damaged erythrocytes (*17*, *18*). This intrinsic biological property positions erythrocytes as ideal carriers for therapeutic delivery specifically to splenic myeloid cells. In addition, erythrocytes exhibit excellent biocompatibility, minimal immunogenicity when derived from O-negative donors, and high availability, further enhancing their suitability as therapeutic vehicles (*19*, *20*). Prior studies using noncovalently attached nanoparticles on erythrocytes have demonstrated their potential to deliver therapeutic molecules to targeted tissues (*21*).

In this study, we hypothesized that engineered erythrocytes could effectively deliver mRNA-loaded nanoparticles directly to splenic myeloid cells, enabling robust in vivo CAR myeloid cell generation. We developed an erythrocyte-mediated mRNA delivery system (mRNA-LNP-Ery), in which mRNA-loaded LNPs were covalently

[1]Key Laboratory of Growth Regulation and Translational Research of Zhejiang Province, School of Life Sciences, Westlake University, Hangzhou, Zhejiang 310030, China. [2]Westlake Laboratory of Life Sciences and Biomedicine, Hangzhou, Zhejiang 310024, China. [3]Research Center for Industries of the Future and School of Life Sciences, Westlake University, Hangzhou, Zhejiang 310030, China. [4]Westlake Therapeutics, Hangzhou, Zhejiang 310024, China. [5]Peking-Tsinghua Center for Life Sciences, Academy for Advanced Interdisciplinary Studies, Peking University, Beijing 100871, China. [6]Ministry of Education Key Laboratory of Cell Proliferation and Differentiation, School of Life Sciences, Peking University, Beijing 100871, China.
†These authors contributed equally to this work.
*Corresponding author. Email: gaoxiaofei@westlake.edu.cn (X.G.); slee@pku.edu.cn (H.-Y.L.)

conjugated to erythrocyte membrane proteins using maleimide-thiol chemistry. We systematically evaluated its biodistribution, cellular uptake mechanisms, and translational efficiency in vivo. Using this platform, we further assessed whether spleen-targeted delivery of mRNA-LNP-Ery could support the generation of functional CAR-expressing myeloid cells, promote immune reprogramming, and elicit antitumor activity in solid tumor models. This study defines the mechanistic and translational potential of erythrocyte-mediated mRNA delivery as a strategy for in vivo immune cell engineering in cancer immunotherapy.

RESULTS

mRNA-LNP delivery by engineered erythrocytes predominantly localizes to the spleen

To engineer erythrocytes as an efficient mRNA delivery platform, we modified commercially available LNPs by incorporating 1,2-distearoyl-sn-glycero-3-phosphoethanolamine (DSPE)–polyethylene glycol, molecular weight 2000 (PEG2000)–maleimide, allowing stable covalent attachment to erythrocyte membrane proteins through maleimide-thiol chemistry (*22*). The final LNP formulation, composed of dilinoleyl-methyl-4-dimethylaminobutyrate (DLin-MC3-DMA), 1,2-distearoyl-sn-glycero-3-phosphocholine (DSPC), cholesterol, 1,2-dimyristoyl-rac-glycero-3-methoxypolyethylene glycol (DMG)-PEG2000, and DSPE-PEG2000-maleimide at a molar ratio of 50:10:38.5:0.75:0.75, was designed to encapsulate *N*1-methylpseudouridine (m1Ψ)–modified mRNA to maximize translation efficiency and minimize immunogenicity (*23*). These maleimide-modified LNPs (mRNA-LNP-Mal) exhibited physicochemical properties similar to those of standard mRNA-LNPs, with an average particle diameter of ~121 nm (table S1). The exposed maleimide moieties on mRNA-LNP-Mal covalently reacted with free thiol groups in the cysteine residues of erythrocyte membrane proteins, forming stable mRNA-LNP-Ery conjugates (Fig. 1A).

Conjugation efficiency was evaluated using Cyanine 5 (Cy5)–labeled luciferase mRNA (Luc-mRNA). Flow cytometry analysis revealed 100% conjugation efficiency, with Cy5 signals detected on all erythrocytes incubated with Luc-LNP-Mal (Fig. 1B). Erythrocyte deformability, phosphatidylserine exposure, and expression of the antiphagocytic marker CD47 remained unchanged compared to unmodified mouse erythrocytes (mEry) or those conjugated with empty LNPs (E-LNP-mEry), indicating that the conjugation process did not compromise erythrocyte integrity (Fig. 1C and fig. S1). Immunofluorescence imaging further confirmed stable attachment of LNPs without morphological changes in erythrocytes (Fig. 1D). Quantitative polymerase chain reaction (qPCR) analysis revealed that an average of 13.4 μg of Luc-mRNA was loaded onto 1×10^{10} erythrocytes (Fig. 1E). Incubation with mRNA-LNPs alone did not yield detectable mRNA signals, confirming that conjugation depends on covalent linkage to erythrocyte membrane proteins.

To assess in vivo delivery efficiency, Luc-LNP-mEry was intravenously administered to C57BL/6 mice, with E-LNP-mEry and free Luc-LNPs serving as controls (Fig. 1F). Luciferase expression was quantified across major organs, including the heart, liver, spleen, lung, kidney, and bone marrow (BM), 18 hours after injection. Consistent with previous studies, Luc-LNP treatment resulted in the highest luciferase activity in the liver compared with other organs (Fig. 1, G and H) (*6*). In contrast, Luc-LNP-mEry produced dominant luciferase activity in the spleen, with minimal expression in other organs (Fig. 1, G and H). Luciferase signal in the spleen of Luc-LNP-mEry–treated mice was ~17.0-fold higher than those in Luc-LNP–treated mice (Fig. 1H). To confirm this spleen-specific delivery, we used LNPs or LNP-Ery encapsulated with Cre recombinase mRNA in C57BL/6 Cre-reporter mice (*H11CAG-loxp-ZsGreen-Stop-loxp-tdTomato*). In these mice, ZsGreen is normally expressed throughout the body, and tdTomato expression is prevented by a loxP-flanked STOP cassette (*24*). After treatment with Cre-LNP-mEry, we observed a 1.86-fold increase in tdTomato expression in the spleens compared with Cre-LNP–treated mice; in contrast, liver signal was reduced to approximately 1/250 of that observed with Cre-LNPs (Fig. 1I).

We next investigated the biodistribution and clearance kinetics of LNP-Ery. Immunofluorescence analysis showed rapid accumulation of both E-LNP-mEry and Luc-LNP-mEry in the spleen at 2 hours postinjection, significantly ($P < 0.01$) exceeding that of unmodified erythrocytes (fig. S2, A and B). By 72 hours postinjection, signals in the spleens were reduced for both LNP-mEry groups, whereas unmodified erythrocytes showed minimal change over time. Correspondingly, peripheral blood analysis indicated a shortened circulation half-life (14.4 to 16.8 hours) for LNP-mEry compared with natural erythrocytes (fig. S2C), consistent with increased splenic retention and phagocytic clearance (*25*).

Aged-, particle-coated, or membrane-modified erythrocytes are typically surveilled and cleared by splenic mononuclear phagocytes (*26*). Given that LNP conjugation did not alter erythrocyte morphology or surface aging markers (Fig. 1C and fig. S1), we hypothesized that the LNPs themselves mediate splenic recognition and uptake. To test this, we performed an in vitro phagocytosis assay in which mouse BM–derived $CD11b^+$ myeloid cells were cocultured with far-red–labeled erythrocytes (fig. S3A). Both E-LNP-mEry and Luc-LNP-mEry were efficiently internalized, whereas unmodified erythrocytes exhibited minimal uptake, as revealed by confocal imaging and flow cytometry (fig. S3B). Given that low-density lipoprotein receptor (LDLR)–ApoE–mediated endocytosis represents a key pathway for free LNP internalization, we next compared mRNA-LNP-Ery uptake in wild-type (WT) and LDLR-deficient ($Ldlr^{-/-}$) mice (*7*). In $Ldlr^{-/-}$ mice, Luc-LNP treatment resulted in markedly reduced hepatic luciferase expression compared with WT controls (fig. S3C). In contrast, Luc-LNP-mEry–mediated expression remained unchanged between WT and $Ldlr^{-/-}$ mice (fig. S3C). This was further validated by in vitro experiments, showing a 68% reduction in Luc-LNP uptake by $CD11b^+$ myeloid cells derived from $Ldlr^{-/-}$ mice compared with WT mice, whereas uptake of Luc-LNP-mEry remained unchanged (fig. S3D). These results indicated that the LNP conjugation triggers erythrocyte recognition by splenic phagocytes through an LDLR-independent, phagocytosis-driven pathway. Together, these results demonstrated that LNP-Ery preferentially directs mRNA delivery to the spleen.

Erythrocyte-mediated mRNA delivery selectively targets splenic $CD11b^+$ myeloid cells

We next characterized the cellular specificity of mRNA expression in splenic immune cells after mRNA-LNP-Ery delivery. In mice treated with Luc-LNP-Ery, luciferase activity was predominantly detected in $CD11b^+$ myeloid cells, with minimal activity in other immune subsets (Fig. 2A). To further validate this specificity, we treated C57BL/6 Cre-reporter mice with either Cre-LNP-Ery or free Cre-LNPs. Our results showed that in the Cre-LNP-mEry group, 66% of $tdTomato^+$ splenocytes were $CD11b^+$ myeloid cells, comprising both $CD11b^+$ $F4/80^+$

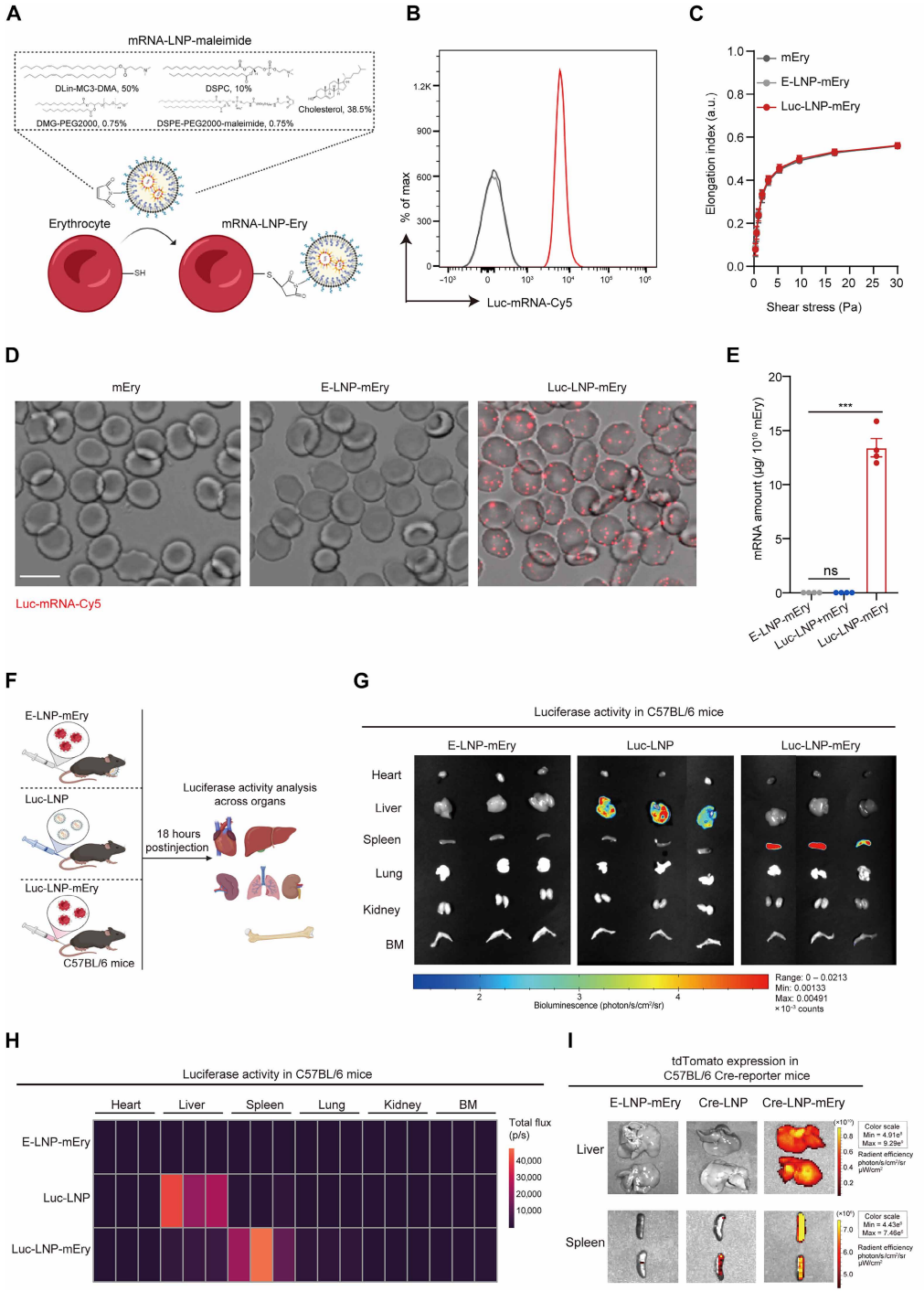

Fig. 1. mRNA-LNP-Ery predominantly targets the spleen for mRNA delivery. (**A**) Schematic illustration of mRNA-LNP-Ery preparation. (**B**) Flow cytometry histogram showing mRNA-Cy5 signal detection for mEry, E-LNP-mEry, and Luc-LNP-mEry. Representative data from three independent experiments. (**C**) Maximum elongation index (EI_{max}) values representing the deformability of mEry, E-LNP-mEry, and Luc-LNP-mEry ($n = 2$ biologically independent samples per group). Representative data from two independent experiments. (**D**) Confocal microscopy images of mEry, E-LNP-mEry, and Luc-LNP-mEry. Representative data from two independent experiments. Scale bar, 10 μm. (**E**) Quantification of Luc-mRNA on erythrocytes, analyzed by reverse transcription qPCR ($n = 4$ biologically independent samples per group). Representative data from three independent experiments. (**F** to **H**) Luciferase activity in major organs from mice after treatment with E-LNP-Ery, Luc-LNP, or Luc-LNP-mEry. (F) Experimental outline. (G) Luminescence images from major organs 18 hours postinjection. (H) Quantification of luminescence in major organs as measured by an in vivo imaging system ($n = 3$ mice per group). (**I**) Cre-LNP and Cre-LNP-mEry–mediated gene expression in Cre-reporter mice visualized by tdTomato expression in the spleens and livers. Mice received the indicated treatments every 3 days, and spleens and livers were isolated 48 hours after the third treatment. tdTomato signals from isolated organs were measured using the in vivo imaging system ($n = 2$ mice per group). Data are presented as means ± SEM. Statistical significance was determined by one-way ANOVA with Tukey's multiple comparisons test (E). ns, not significant; ***$P < 0.001$. a.u., arbitrary unit; max, maximum; min, minimum.

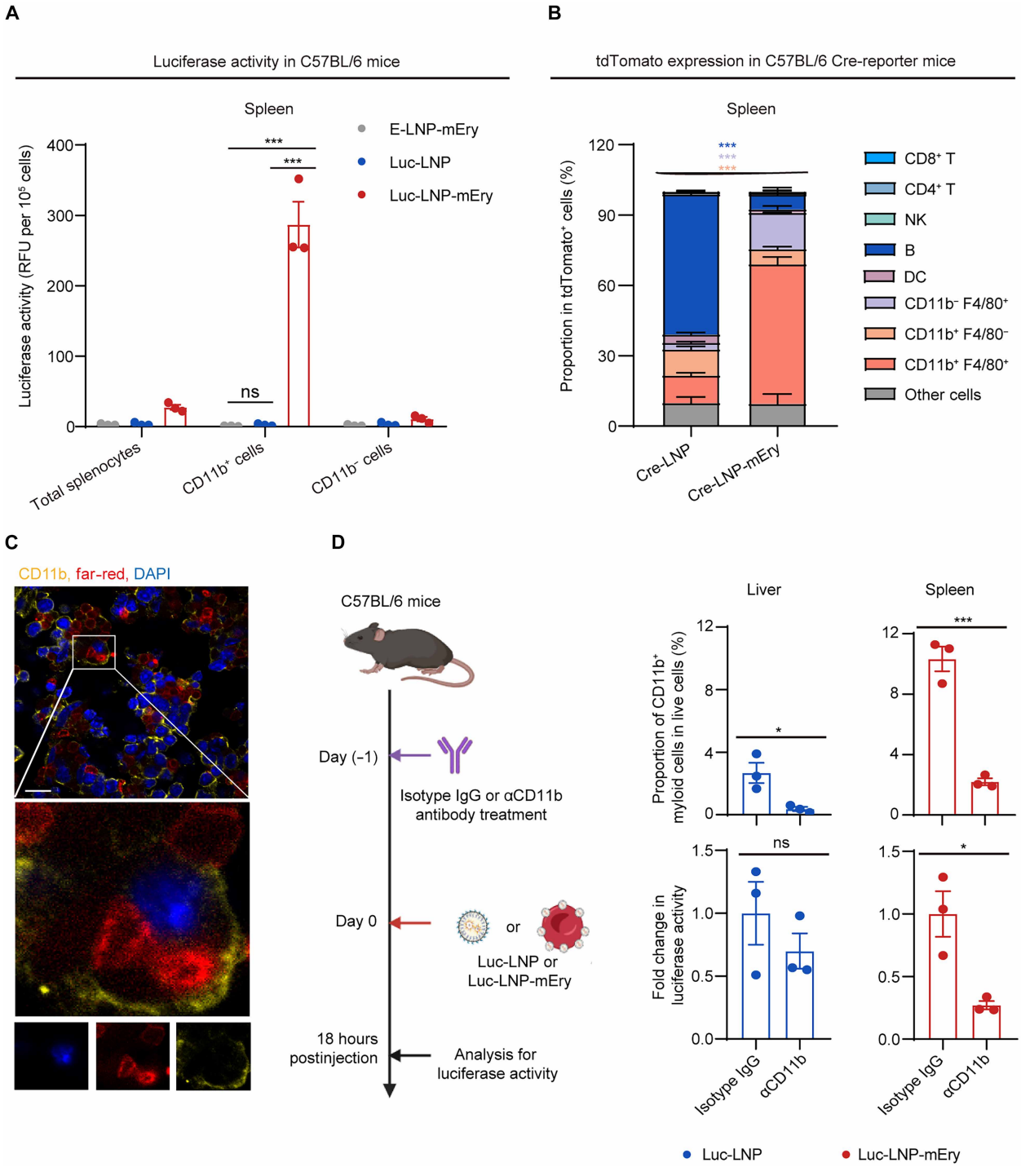

Fig. 2. mRNA-LNP-Ery selectively delivers mRNA into splenic CD11b$^+$ myeloid cells. (**A**) Luciferase activity in splenocytes from C57BL/6 mice treated with E-LNP-mEry, Luc-LNPs, or Luc-LNP-mEry. Splenocytes were isolated 18 hours postadministration, and luciferase activity was measured by luminescence assay ($n = 3$ mice per group). (**B**) Proportion of tdTomato$^+$ splenocytes in Cre-reporter mice treated with Cre-LNPs or Cre-LNP-mEry, analyzed by flow cytometry ($n = 3$ mice per group). (**C**) Immunofluorescence analysis of Luc-LNP-mEry uptake by CD11b$^+$ splenic myeloid cells. Scale bar, 10 μm. Images are representative of two independent experiments. (**D**) C57BL/6 mice were treated with either an αCD11b depletion antibody or an isotype immunoglobulin G (IgG) antibody 1 day before receiving the treatments, after which livers and spleens were isolated to quantify luminescence from the different groups. Proportions of CD11b$^+$ myeloid cells in live cells (top, as measured by flow cytometry) and fold changes in luciferase activity (bottom, as measured by an in vivo imaging system) from different groups are shown ($n = 3$ mice per group). Data are presented as means ± SEM. Statistical significance was determined by two-way ANOVA with Tukey's multiple comparisons test (A), two-way ANOVA with Šidák's multiple comparisons test (B), or unpaired *t* test (D). ns, not significant; $^*P < 0.05$; $^{***}P < 0.001$. DAPI, 4′,6-diamidino-2-phenylindole; RFU, relative fluorescence units.

and CD11b$^+$ F4/80$^-$ subsets (Fig. 2B). The remaining fractions of td-Tomato$^+$ cells included tissue-resident macrophages [red pulp macrophages (RPMs), CD11b$^-$ F4/80$^+$, ~16%], dendritic cells [DCs; CD11c$^+$ major histocompatibility complex class II–positive (MHC-II$^+$), ~2%], lymphocytes (~1%), and other populations (~10%). In contrast, only ~20% of tdTomato$^+$ cells were CD11b$^+$ myeloid cells in mice treated with free Cre-LNPs (Fig. 2B).

To examine the interaction of mRNA-LNP-Ery with CD11b$^+$ myeloid cells, Luc-LNP-mEry was labeled with a far-red fluorescent dye prior to injection into C57BL/6 mice. At 2 hours postinjection, imaging revealed active phagocytosis of fluorescently labeled mRNA-LNP-mEry by splenic CD11b$^+$ myeloid cells (Fig. 2C). To confirm the critical role of CD11b$^+$ myeloid cells in mRNA delivery by erythrocytes, we depleted these cells using an anti-CD11b antibody prior to administration (Fig. 2D). Compared with the control group, luciferase activity in the spleens was reduced by over 70% in CD11b$^+$ cell–depleted mice (Fig. 2D). By comparison, CD11b$^+$ cell depletion had no significant effect on liver gene expression in Luc-LNP–treated mice, because LNP uptake in the liver is primarily mediated by hepatic cells (Fig. 2D) (*27*). Together, these findings demonstrated that splenic CD11b$^+$ myeloid cells are the primary cellular targets of erythrocyte-based mRNA delivery.

Erythrocyte-mediated mRNA delivery enhances mRNA expression efficiency through phagocytosis

Conventional LNPs enter cells through receptor-mediated endocytosis, which often leads to endosomal sequestration and limited cytosolic mRNA release (*6*). Because erythrocytes are naturally cleared by myeloid cells through an actin-dependent process distinct from endocytosis (*28*), we asked whether erythrocyte-mediated delivery could use phagocytosis to overcome this intracellular bottleneck. To test this, mouse BM–derived CD11b$^+$ myeloid cells were pretreated with cytochalasin D, an actin polymerization inhibitor, before exposure to Luc-LNP-mEry carrying Cy5-labeled Luc-mRNA (*29*). Our results showed that cytochalasin D reduced Luc-LNP-mEry internalization by 11.1-fold, indicating that actin-dependent phagocytosis is the dominant entry route for mRNA-LNP-Ery (fig. S4, A and B). We next compared mRNA delivery efficiency between Luc-LNPs and Luc-LNP-mEry. CD11b$^+$ myeloid cells were incubated with either Luc-LNPs or Luc-LNP-mEry containing Cy5-mRNA (Fig. 3A). Flow cytometry showed comparable cellular uptake of Cy5-mRNA with both treatments, whereas luciferase activity was 7.6-fold higher with Luc-LNP-mEry (Fig. 3B), indicating that erythrocyte-mediated delivery enhances cytosolic mRNA release and translation efficiency.

To further elucidate the intracellular trafficking pathway, we performed time-resolved confocal microscopy using early endosomal antigen-1 (EEA-1) and lysosomal-associated membrane protein-1 (LAMP-1) as markers of endosomal and phagosomal maturation (*30, 31*). As expected, conventional LNPs exhibited sustained endosomal sequestration, with Cy5-mRNA strongly colocalized with EEA-1 (43.7 to 58.0%) and LAMP-1 (71.5 to 77.7%) at 6 to 12 hours (Fig. 3C) (*9*). For mRNA-LNP-Ery, we tracked the erythrocyte moiety and the mRNA cargo in parallel by labeling erythrocytes with a far-red dye and mRNA with Cy5. The far-red signal indicated that erythrocytes were initially confined within EEA-1$^+$ phagosomes at 2 hours, began to overlap with LAMP-1 compartments at 6 hours, and, by 16 hours, showed a marked decline in far-red intensity and appeared as fragmented structures colocalized with EEA-1 (31.9%) and LAMP-1 (53.7%), indicating progressive phagosome maturation and erythrocyte degradation (Fig. 3, D and E). The Cy5-labeled mRNA signal showed that the conjugated mRNA-LNPs were internalized together with erythrocytes through phagocytosis and remained associated up to 6 hours; by 16 hours, mRNA was largely dissociated from erythrocyte remnants and exhibited minimal colocalization (<10%) with either EEA-1 or LAMP-1 (Fig. 3, D and E), indicating that a substantial fraction of mRNA had escaped from phagosomes, thereby enabling enhanced cytosolic release for translation. Together, these findings demonstrated that mRNA-LNP-Ery enters myeloid cells through phagocytosis and releases its mRNA cargo into the cytosol before phagolysosomal degradation. This alternative uptake pathway bypasses endosomal trapping, leading to markedly improved mRNA delivery and protein expression compared with conventional LNPs.

Characterization of CAR myeloid cells generated by mRNA-LNP-Ery in vivo

Splenic CD11b$^+$ myeloid cells can migrate to peripheral blood, tumors, or other diseased tissues, where they differentiate into M1 macrophages capable of phagocytosis and antigen presentation (*32, 33*). In addition, expressing CARs such as anti–human epidermal growth factor receptor 2 (HER2) CAR in human macrophages or monocytes can redirect their phagocytic function, leading to targeted antitumor effects and the stimulation of adaptive immune responses (*1, 34*). We therefore investigated whether systemic delivery of anti-HER2-CAR mRNA using erythrocytes could generate therapeutic CAR myeloid cells in vivo.

We designed the anti-HER2-CAR construct, incorporating the anti-HER2 scFv (derived from herceptin), a mouse CD8 transmembrane (TM) domain, and the mouse CD3ζ intracellular domain (Fig. 4A) (*35*). The CD3ζ shares homology with the Fc common γ-chain (FcεRI-γ), a canonical signaling molecule for antibody-dependent cellular phagocytosis in macrophages (*30*). To enhance the phagocytic capacity of myeloid cells, we incorporated a phosphatidylinositol 3-kinase (PI3K) recruitment domain, which is essential for the internalization of large targets such as tumor cells (*31*). Transducing this construct into RAW 264.7 macrophage cells confirmed its functionality, as shown by antigen-specific phagocytosis of HER2$^+$ beads (Fig. 4B).

We next delivered anti-HER2-CAR mRNA by erythrocytes (HER2-CAR-LNP-mEry) in a syngeneic MC38-hHER2 colorectal cancer model, in which murine MC38 tumor cells are engineered to stably express human HER2, and profiled splenic myeloid subsets for uptake and expression using established gating strategies (*26*, *36*). Macrophage subsets included RPMs (CD11b$^-$ F4/80$^+$), marginal metallophilic macrophages (MMMs; F4/80$^-$ CD169$^+$), and marginal zone macrophages (MZMs; F4/80$^-$ CD209b$^+$) (fig. S5). Monocytes were subdivided into inflammatory monocytes (CD11b$^+$ Ly6C$^+$ F4/80$^+$ and CD11b$^+$ Ly6C$^+$ F4/80$^-$) and precursor RPMs (Pre-RPMs; CD11b$^+$ F4/80$^+$ Ly6C$^-$) (fig. S5). At 18 hours postinjection, CD11b$^+$ Ly6C$^+$ monocytes (both F4/80$^+$ and F4/80$^-$) were the predominant population internalizing far-red–labeled HER2-CAR-LNP-mEry, with ~50% of cells showing uptake (fig. S6A). Among these far-red$^+$ CD11b$^+$ Ly6C$^+$ monocytes, ~60 to 70% expressed detectable HER2-CAR protein, corresponding to ~20 to 30% of total CD11b$^+$ Ly6C$^+$ monocytes in the spleen being CAR$^+$ (fig. S6A and Fig. 4C). In contrast, Pre-RPMs and tissue-resident macrophages (RPMs, MMMs, and MZMs) also internalized HER2-CAR-LNP-mEry but exhibited markedly lower CAR expression (<5%) (fig. S6A and Fig. 4C). In total, HER2-CAR-LNP-mEry generated ~3.1×10^5 CAR$^+$ myeloid cells per spleen, ~95%

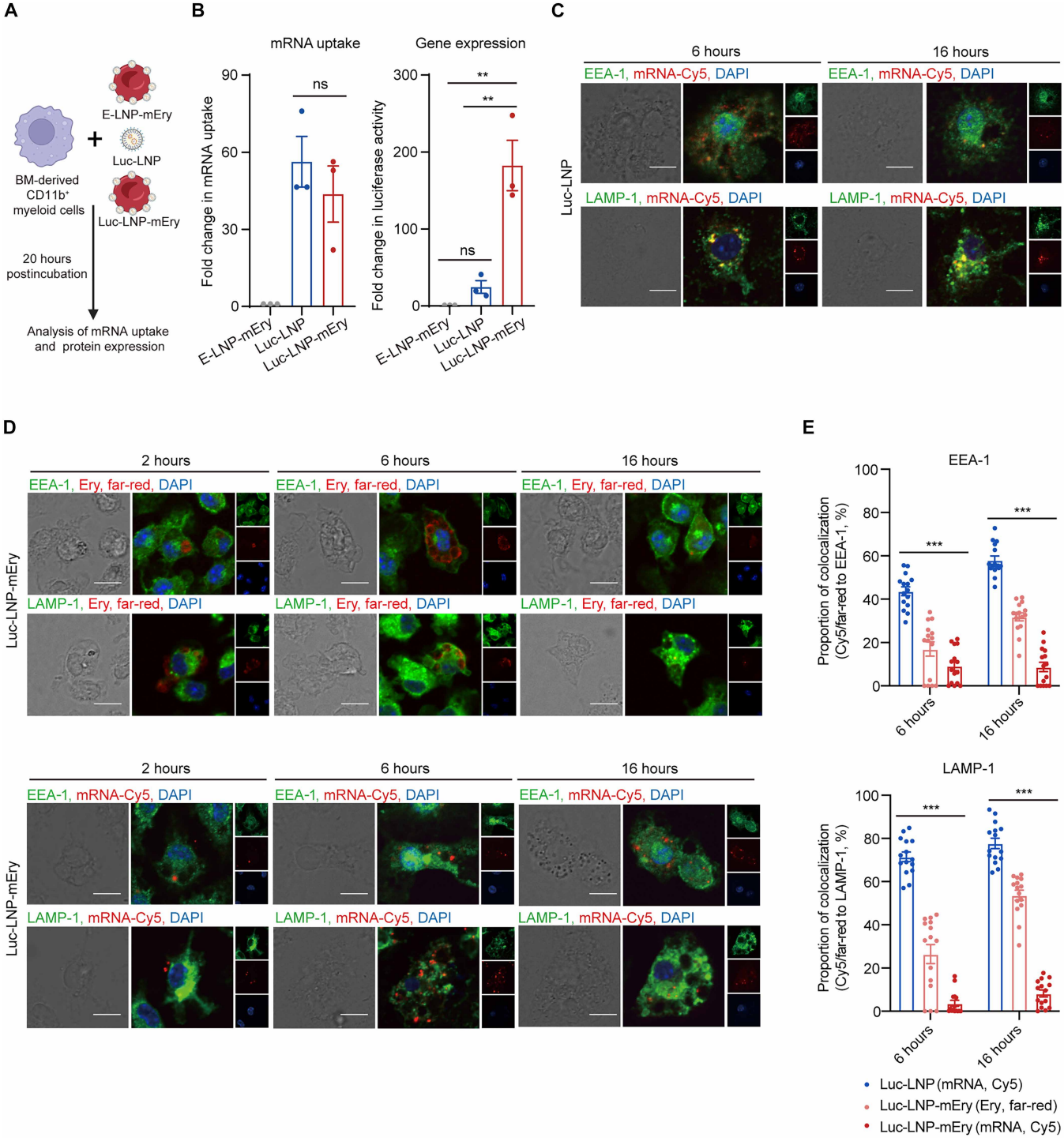

Fig. 3. mRNA-LNP-Ery bypasses endosomal trapping and enhances mRNA translation efficiency. (**A**) Experimental schematic showing coculture of CD11b$^+$ myeloid cells with E-LNP-mEry, Luc-LNPs, or Luc-LNP-mEry. (**B**) Quantification of Cy5-mRNA uptake (as measured by flow cytometry) and luciferase activity (as measured by luminescence assay) in CD11b$^+$ myeloid cells after treatment with the indicated formulations ($n = 3$ biologically independent samples per group). Representative data from two independent experiments. (**C** to **E**) CD11b$^+$ myeloid cells were cocultured with Luc-LNPs or Luc-LNP-mEry and analyzed by immunofluorescence at the indicated time points ($n = 3$ biologically independent samples per group, with five cells analyzed per sample). (C) Representative immunofluorescence images showing Cy5-labeled mRNA delivered by Luc-LNPs and EEA-1 or LAMP-1 staining at 6 and 16 hours posttreatment. Scale bars, 10 μm. (D) Top: Representative immunofluorescence images showing far-red–labeled erythrocytes with EEA-1 or LAMP-1 staining at 2, 6, and 16 hours posttreatment. Bottom: Representative immunofluorescence images showing Cy5-labeled mRNA delivered by Luc-LNP-mEry with EEA-1 or LAMP-1 staining at 2, 6, and 16 hours posttreatment. Scale bars, 10 μm. (E) Quantitative colocalization analysis of Cy5 (mRNA signal) or far-red (erythrocyte signal) with EEA-1 or LAMP-1 based on (C) and (D). Data are presented as means ± SEM. Statistical significance was determined by one-way ANOVA with Tukey's multiple comparisons test (B), or two-way ANOVA with Šidák's multiple comparisons test (E). ns, not significant; $^{**}P < 0.01$; $^{***}P < 0.001$.

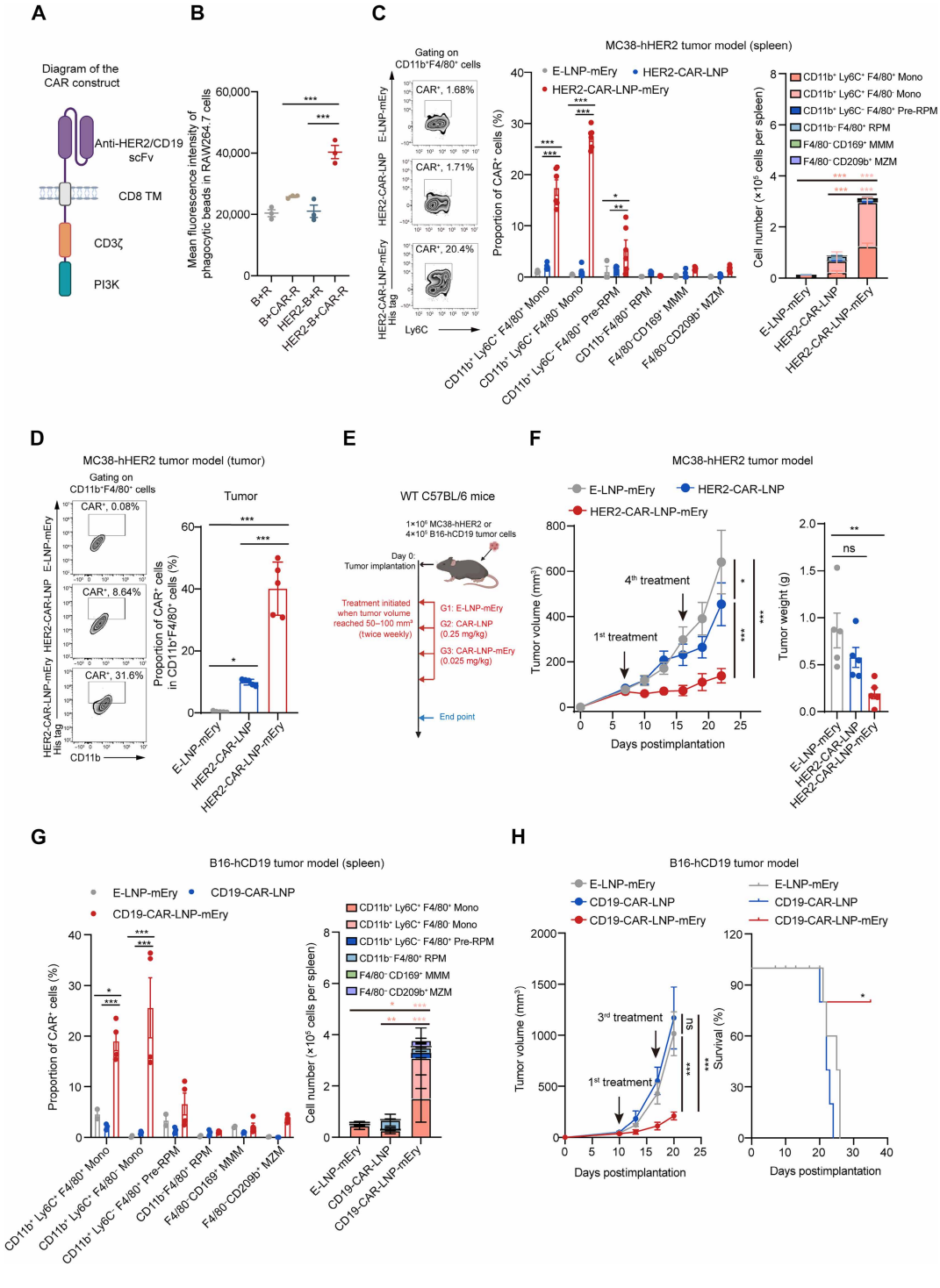

Fig. 4. CAR myeloid cells generated by CAR-LNP-Ery achieve potent antitumor activity. (**A**) Schematic diagram of the CAR constructs targeting HER2 or CD19. (**B**) RAW 264.7 cells (R) transduced with or without HER2-CAR mRNA were subjected to bead-based phagocytosis analysis ($n = 3$ biologically independent samples per group). Representative data from two independent experiments. (**C** and **D**) MC38-hHER2 tumor–bearing mice were treated with E-LNP-mEry, HER2-CAR-LNP, or HER2-CAR-LNP-mEry. Spleens and tumors were harvested for flow cytometry analysis 18 hours postinjection. (C) Flow cytometry analysis of HER2-CAR expression in splenic myeloid subsets from MC38-hHER2 tumor–bearing mice treated with E-LNP-mEry, HER2-CAR-LNP, or HER2-CAR-LNP-mEry ($n = 3$ mice for E-LNP-mEry, $n = 6$ mice for HER2-CAR-LNP, and $n = 6$ mice for HER2-CAR-LNP-mEry). Left: Representative plots showing HER2-CAR expression in $CD11b^+$ $F4/80^+$ $Ly6C^+$ monocytes. Middle: Proportions of $HER2\text{-}CAR^+$ cells within each splenic myeloid subset. Right: Total numbers of $HER2\text{-}CAR^+$ myeloid cells per spleen. (D) Flow cytometry analysis of HER2-CAR expression in tumor-infiltrating myeloid cells ($n = 5$ mice per group). Left: Representative CAR expression in $CD11b^+$ $F4/80^+$ cells. Right: Proportions of $HER2\text{-}CAR^+$ cells in $CD11b^+$ $F4/80^+$ myeloid cells. (**E**) Experimental outline illustrating the evaluation of antitumor efficacy of CAR-LNP-Ery in tumor models. (**F**) Antitumor efficacy of E-LNP-mEry, HER2-CAR-LNPs, or HER2-CAR-LNP-mEry in mice bearing subcutaneous MC38-hHER2 tumors. C57BL/6 mice were treated twice weekly beginning 7 days post tumor implantation. Tumor growth (left) and tumor weight (right) were recorded in MC38-hHER2 tumor-bearing C57BL/6 mice ($n = 5$ mice per group). (**G**) B16-hCD19 tumor–bearing mice were treated with E-LNP-mEry, CD19-CAR-LNPs, or CD19-CAR-LNP-mEry. Spleens were harvested for flow cytometry analysis 18 hours postinjection. Flow cytometry analysis of CD19-CAR expression in splenic myeloid subsets from B16-hCD19 tumor–bearing mice treated with E-LNP-mEry, CD19-CAR-LNPs, or CD19-CAR-LNP-mEry ($n = 2$ mice for E-LNP-mEry, $n = 3$ mice for CD19-CAR-LNPs, and $n = 4$ mice for CD19-CAR-LNP-mEry). Left: Proportions of $CD19\text{-}CAR^+$ cells within each splenic myeloid subset. Right: Total numbers of $CD19\text{-}CAR^+$ myeloid cells per spleen. (**H**) Antitumor efficacy of E-LNP-mEry, CD19-CAR-LNP, or CD19-CAR-LNP-mEry in mice bearing subcutaneous B16-hCD19 tumors. C57BL/6 mice were treated twice weekly beginning 10 days post tumor implantation ($n = 5$ mice per group). Tumor growth (left) and survival curves (right) were recorded. Data are presented as means ± SEM. Statistical significance was determined by one-way ANOVA with Tukey's multiple comparisons test [(B), (D), and (F), right], two-way ANOVA with Šidák's multiple comparisons test [(C), middle, and (G), left], two-way ANOVA with Tukey's multiple comparisons test [(C), right; (F), left; (G), right; and (H), left], or log-rank (Mantel-Cox) test [(H), right]. ns, not significant; $*P < 0.05$; $**P < 0.01$; $***P < 0.001$. B, beads; HER2-B, HER2 antigen–conjugated beads; CAR-R, mRNA encoding HER2-CAR; G, group.

of which were CD11b$^+$ Ly6C$^+$ monocytes, a 3.6-fold increase compared with HER2-CAR-LNP treatment, despite using only one-tenth of the mRNA dose (Fig. 4C and fig. S6B).

We then systematically analyzed HER2-CAR expression in extrasplenic compartments. Myeloid cells in the liver and lung exhibited moderate uptake (<20%) but low CAR expression (<5%), whereas lymph node myeloid cells showed minimal uptake (<0.5%), likely because of limited vascular accessibility (fig. S6C). In contrast, abundant HER2-CAR$^+$ CD11b$^+$ F4/80$^+$ cells were detected in tumors, indicating active migration of splenic CAR myeloid cells to tumor sites (Fig. 4D). Last, we evaluated the persistence of these in vivo–generated CAR myeloid cells and found that HER2-CAR expression within each myeloid subset, as well as the total number of CAR$^+$ myeloid cells, declined to below 30% of the initial amount by 72 hours posttreatment (fig. S6, D and E).

CAR myeloid cells generated by mRNA-LNP-Ery exhibit potent antitumor activity with high safety

We next evaluated the antitumor activity of HER2-CAR-LNP-mEry in MC38-hHER2 tumor models (Fig. 4E) (*2*). Given the ~3-day persistence of CAR expression in splenic myeloid cells, mice were treated every 3 days once tumors reached ~100 mm^3 (fig. S6, D and E). Although HER2-CAR-LNPs induced only a modest antitumor response, HER2-CAR-LNP-mEry significantly ($P < 0.001$) suppressed tumor growth, resulting in an 80% reduction in tumor size (Fig. 4F). In addition, HER2-CAR-LNP-mEry required only 0.5 μg of mRNA, one-tenth the dose used in the HER2-CAR-LNP group, further highlighting the efficiency of spleen-targeted delivery. To further validate the role of the spleen in the antitumor effects of HER2-CAR-LNP-mEry, we performed splenectomy and evaluated the antitumor activity of the treatment. We failed to detect HER2-CAR$^+$ CD11b$^+$ myeloid cells in splenectomized mice treated with HER2-CAR-LNP-mEry (fig. S7A). The antitumor effect was also completely abolished in splenectomized mice bearing tumors, suggesting that the spleen is critical for HER2-CAR-LNP-Ery's function (fig. S7, B and C).

To evaluate the functional activity of in vivo–generated CAR myeloid cells in immune "cold" tumors, we used a macrophage-rich and T cell–poor B16-hCD19 melanoma model, in which B16 melanoma cells are engineered to express human CD19, and used erythrocytes to deliver mRNA encoding an anti-CD19 CAR designed analogously to the anti-HER2-CAR (Fig. 4A) (*37*, *38*). Consistently, CD19-CAR-LNP-mEry efficiently generated ~4 × 10^5 CAR$^+$ myeloid cells per spleen, over 80% of which were CD11b$^+$ Ly6C$^+$ monocytes (Fig. 4G). Once tumors reached ~50 mm^3, mice were treated with E-LNP-mEry, CD19-CAR-LNPs, or CD19-CAR-LNP-mEry. Although CD19-CAR-LNPs alone showed no significant efficacy, CD19-CAR-LNP-mEry treatment resulted in marked tumor regression (75% reduction in tumor size) and prolonged survival (Fig. 4H), validating the functional activity of CAR myeloid cells beyond the HER2 setting. Depletion of macrophages and monocytes using a colony-stimulating factor 1 receptor (CSF1R)–depleting antibody administered 2 hours after each CD19-CAR-LNP-mEry dose abolished the antitumor efficacy of CD19-CAR-LNP-mEry, confirming that the myeloid compartment mediates the therapeutic effect (fig. S8) (*39*, *40*).

Furthermore, we evaluated the safety of CAR-LNP-mEry. Consistent with previous reports, repeated administration of conventional HER2-CAR-LNPs induced systemic toxicity, including body weight loss, splenomegaly, elevated serum alanine aminotransferase and aspartate aminotransferase, and increased interleukin-6 secretion (fig. S9, A to C) (*41*). In contrast, HER2-CAR-LNP-mEry caused minimal side effects, likely due to its lower dosages and selective targeting of the spleen, thereby avoiding systemic distribution associated with current LNP systems (fig. S9, A to C). Collectively, these findings demonstrated that erythrocyte-mediated delivery effectively generates CAR myeloid cells in vivo, eliciting durable antitumor responses with a substantially improved safety profile.

CAR myeloid cells generated by mRNA-LNP-Ery adopt a proinflammatory phenotype that enhances immune activation

To investigate how CAR-LNP-Ery modulates the splenic immune system, we performed single-cell RNA sequencing (scRNA-seq) on splenocytes harvested 20 hours after treatment from MC38-hHER2 tumor–bearing mice across treatment groups (Fig. 5A and fig. S10A). Within the macrophage/monocyte (Macro/Mono) cluster, we observed pronounced induction of inflammatory and antigen-presentation programs in the HER2-CAR-LNP-Ery group. Gene ontology (GO) enrichment analysis revealed that interferon-response and antiviral pathways were among the most enriched, with increased expression of interferon-stimulated genes, including *Isg15*, *Isg20*, *Ifit1*, and *Oasl1*, together with antigen-presentation genes, including *H2-Eb1*, *H2-Ab1*, and *H2-Q7* (Fig. 5, B and C) (*42*, *43*). Conversely, immunosuppressive mediators, such as *Tgfb1*, *Il1b*, and *Klf4*, were down-regulated in the same population (Fig. 5C) (*42*). DCs and neutrophils displayed concordant transcriptional shifts toward an inflammatory phenotype, indicating broad reprogramming of the splenic myeloid compartment (fig. S10, B and C).

Enrichment analysis of Macro/Mono cells further revealed activation of lymphocyte proliferation and signaling pathways after HER2-CAR-LNP-Ery treatment, suggesting enhanced cross-talk with adaptive immunity (Fig. 5B) (*1*). Consistent with this, splenic CD8$^+$ T cells exhibited increased activation and cytotoxicity signatures, including elevated *Cd69*, *Prf1*, *Isg15*, and *Irf7* expression (Fig. 5, D and E). Similar signatures appeared in CD4$^+$ T cells and natural killer (NK) cells (fig. S10, D and E). Flow cytometry also validated that CD11b$^+$ F4/80$^+$ myeloid cells from the HER2-CAR-LNP-Ery group expressed higher MHC-II and CD86 than controls, consistent with an immunostimulatory, antigen-presenting state (Fig. 5F). In parallel, the frequency of myeloid-derived suppressor cells (MDSCs) was reduced, indicating a shift away from an immunosuppressive state, accompanied by a significant ($P < 0.01$) expansion of effector CD8$^+$ T cells, reflecting enhanced lymphocyte activation (Fig. 5F) (*42*). Collectively, these results demonstrated that CAR-LNP-Ery reprograms splenic myeloid cells toward a proinflammatory, antigen-presenting state and, through this remodeling, promotes lymphocyte activation.

In vivo–generated CAR myeloid cells reprogram the tumor microenvironment and induce systemic antitumor immunity

CAR myeloid cells generated by HER2-CAR-LNP-mEry also profoundly reprogrammed the tumor microenvironment (TME), promoting immune activation characterized by increased infiltration of T cells and NK cells and a concomitant reduction in myeloid and B cell populations, as revealed by scRNA-seq (Fig. 6, A and B, and fig. S11A). Consistent with their splenic counterparts, the Macro/Mono cluster from HER2-CAR-LNP-mEry–treated tumors exhibited strong enrichment of innate immune activation pathways compared with control groups, including elevated expression of proinflammatory genes (*Isg15*, *Irf7*, *Ifit1*, and *Junb*), antigen-presentation genes (*B2m* and *H2-T22*), and

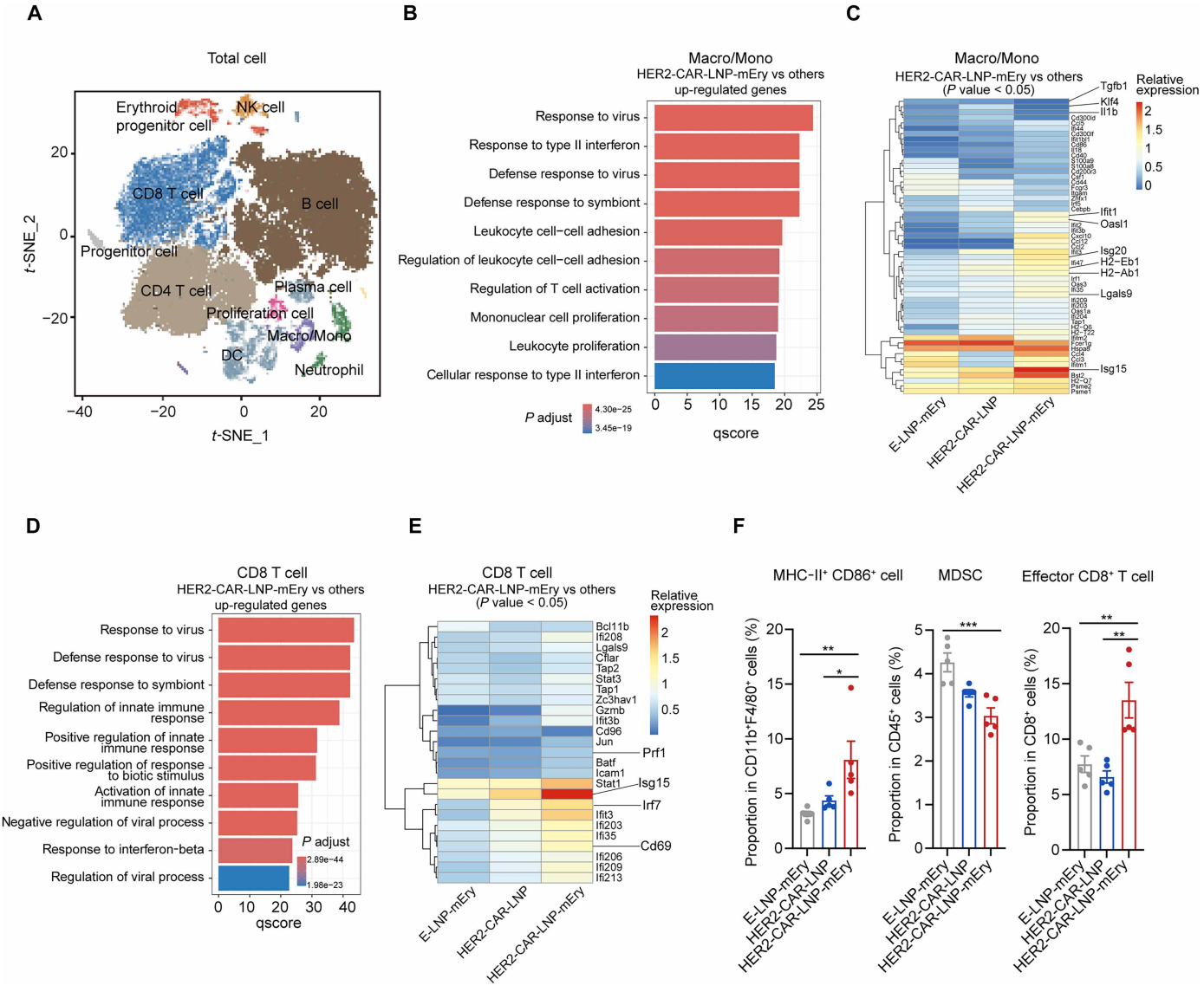

Fig. 5. CAR myeloid cells generated by CAR-LNP-Ery exhibit a proinflammatory phenotype and enhance lymphocyte activation within the spleen. (**A** to **E**) Spleens from one mouse per group were collected from MC38-hHER2 tumor–bearing C57BL/6 mice 20 hours after the third treatment with the indicated formulations and analyzed by scRNA-seq. (A) Combined *t*-distributed stochastic neighbor embedding (*t*-SNE) plot of splenocytes from different treatment groups analyzed by scRNA-seq. (B) GO enrichment analysis showing the top up-regulated pathways in Macro/Mono population from the HER2-CAR-LNP-mEry group compared with other groups. (C) Differentially expressed genes (DEGs) in Macro/Mono population across the three treatment groups. (D) GO enrichment analysis showing the top up-regulated pathways in CD8 T cell population from the HER2-CAR-LNP-mEry group compared with other groups. (E) DEGs in CD8 T cell population across the three treatment groups. (**F**) MC38-hHER2 tumor–bearing C57BL/6 mice were treated as described in Fig. 4F, and spleens were isolated at the study end point for flow cytometry analysis ($n = 5$ mice per group). Left: Proportions of CD86$^+$ MHC-II$^+$ cells among CD11b$^+$ F4/80$^+$ splenic myeloid cells. Middle: Proportions of MDSCs among CD45$^+$ splenocytes. Right: Proportions of effector CD8$^+$ T cells (CD44$^+$ CD62L$^-$) among total CD8$^+$ T cells. Data are presented as means ± SEM. Statistical significance was determined by one-way ANOVA with Dunnett's multiple comparisons test (F). *$P < 0.05$; **$P < 0.01$; ***$P < 0.001$.

phagocytosis-associated genes (*Rab7b* and *Lgals9*), accompanied by reduced expression of immunosuppressive markers (*Mrc1* and *Arg1*) (Fig. 6, C and D). Similar transcriptional activation was observed in DCs (fig. S11B). Flow cytometry further confirmed these findings, showing increased MHC-II and CD86 expression in CD11b$^+$ F4/80$^+$ myeloid cells and a reduction of MDSCs in tumors from HER2-CAR-LNP-mEry–treated mice (Fig. 6E).

Within T cell clusters, we observed enrichment of activation and cytotoxicity pathways, accompanied by up-regulation of effector-associated genes (*Cd69*, *Irf7*, *Isg15*, and *Klf2*) and down-regulation of inhibitory and exhaustion-associated markers (*Pdcd1*, *Klre1*, and *Tox*), consistent with a highly activated effector phenotype (Fig. 6, F and G, and fig. S11C). NK cells similarly displayed enrichment of metabolic and activation programs, indicative of a hyperactivated state (Fig. 6H). These transcriptional findings were validated by flow cytometry and immunohistochemistry, which revealed robust infiltration of CD8$^+$ T cells and NK cells into tumors (Fig. 6, I and J). In splenectomized mice, the immunostimulatory effects of HER2-CAR-LNP-Ery were

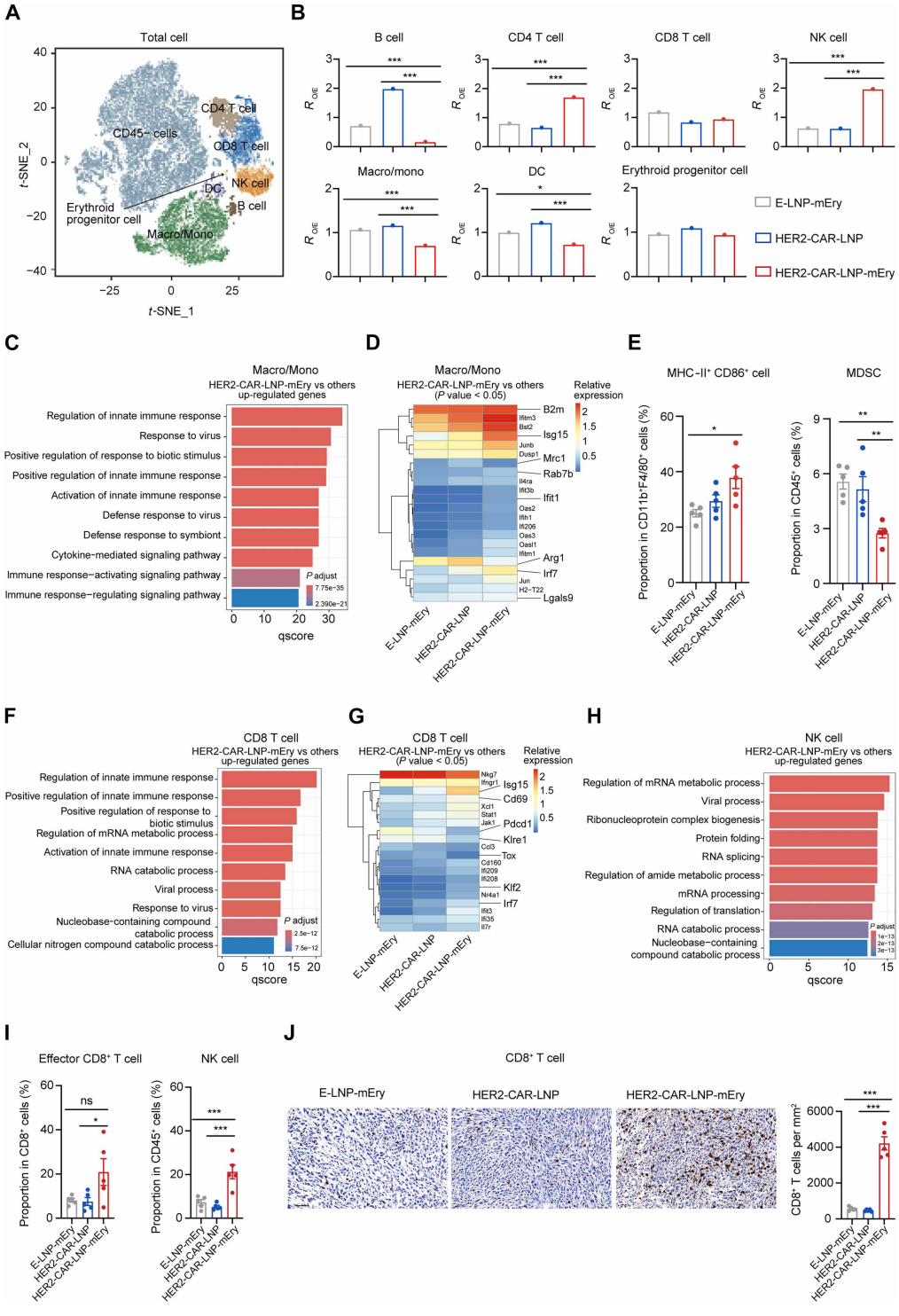

Fig. 6. In vivo–generated CAR myeloid cells reprogram the TME. (**A** to **D**) Tumors from one mouse per group were collected from MC38-hHER2 tumor–bearing C57BL/6 mice 20 hours after the third treatment with the indicated formulations and analyzed by scRNA-seq. (A) Combined *t*-SNE plot of total tumor cells from different treatment groups analyzed by scRNA-seq. (B) Sample preference of each cluster estimated by the ratio of observed to expected ($R_{O/E}$) values. (C) GO enrichment analysis showing the top up-regulated pathways in Macro/Mono population from the HER2-CAR-LNP-mEry group compared with other groups. (D) DEGs in Macro/Mono populations across the three treatment groups. (**E**) Flow cytometry analysis of tumor-infiltrating myeloid cells from MC38-hHER2 tumor–bearing C57BL/6 mice treated as described in Fig. 4F ($n = 5$ mice per group). Left: Proportions of $CD86^+$ $MHC\text{-}II^+$ cells among $CD11b^+$ $F4/80^+$ myeloid cells. Right: Proportions of MDSCs among $CD45^+$ cells. (**F** to **H**) Tumor samples corresponding to (A) to (D) were analyzed by scRNA-seq. (F) GO enrichment analysis showing the top up-regulated pathways in CD8 T cell population from the HER2-CAR-LNP-mEry group compared with other groups. (G) DEGs in CD8 T cell population across the three treatment groups. (H) GO enrichment analysis showing the top up-regulated pathways in NK cell population from the HER2-CAR-LNP-mEry group compared with other groups. (**I**) Flow cytometry analysis of effector lymphocyte populations in MC38-hHER2 tumor–bearing C57BL/6 mice treated as described in Fig. 4F ($n = 5$ mice per group). Left: Proportions of effector $CD8^+$ T cells ($CD44^+$ $CD62L^-$) among total $CD8^+$ T cells. Right: Proportions of NK cells ($NK1.1^+$) among $CD45^+$ tumor cells. (**J**) Immunohistochemistry analysis of tumor sections showing $CD8^+$ T cell infiltration. Left: Representative images from different treatment groups. Scale bar, 50 μm. Right: Quantification of $CD8^+$ T cells ($n = 5$ mice per group). Data are presented as means ± SEM. Statistical significance was determined by two-tailed chi-square test (B) or one-way ANOVA with Dunnett's multiple comparisons test [(E), (I), and (J)]. $^*P < 0.05$; $^{**}P < 0.01$; $^{***}P < 0.001$.

completely abolished, confirming the spleen as the essential site for CAR myeloid generation and systemic immune activation (fig. S7, D and E).

To functionally define the effector populations responsible for tumor control, we evaluated the therapeutic activity of CAR-LNP-Ery in lymphocyte-deficient nude mice, which represent a simplified system lacking adaptive immunity. In MC38-hHER2 tumor–bearing nude mice, HER2-CAR-LNP-mEry treatment still suppressed tumor growth, indicating that CAR myeloid cells have intrinsic tumoricidal activity (fig. S12). However, the antitumor effect was substantially stronger in immunocompetent mice, suggesting a synergistic interplay between CAR myeloid cells and adaptive immune components (Fig. 4F). To further validate this synergy, we performed immune cell depletion studies. Mice received αCD8 or

αNK1.1 antibodies 1 day before each administration of CAR-LNP-mEry. Depletion of either $CD8^+$ T cells or NK cells markedly reduced the efficacy of CD19-CAR-LNP-mEry, decreasing tumor inhibition from 70.0 to ~40%, demonstrating that both populations are critical contributors to its antitumor activity (fig. S8). Together, these findings demonstrated that erythrocyte-mediated mRNA delivery generates functional CAR myeloid cells that reprogram both the splenic immune environment and TME. By coordinating innate and adaptive immune activation, CAR-LNP-Ery elicits a potent systemic antitumor response, underscoring its broad therapeutic potential.

DISCUSSION

In this study, we established a cell-based mRNA delivery strategy by covalently conjugating mRNA-loaded LNPs to erythrocytes, creating a platform termed mRNA-LNP-Ery. This system exploits the natural splenic homing and immune surveillance of erythrocytes to achieve highly selective and efficient mRNA delivery to splenic $CD11b^+$ myeloid cells, such as $CD11b^+$ $Ly6C^+$ monocytes. Mechanistically, mRNA-LNP-Ery enters cells through phagocytosis rather than endocytosis, bypassing endosomal sequestration and enabling robust cytosolic mRNA translation. Using this approach, we generated functional CAR myeloid cells in vivo that not only exhibited intrinsic tumoricidal activity but also reprogrammed the splenic and tumor immune environments to coordinate innate and adaptive immune activation, leading to potent antitumor efficacy with minimal systemic toxicity.

CAR-based cellular therapies, including CAR T and CAR myeloid cells, have shown transformative potential for cancer immunotherapy. However, ex vivo CAR cell engineering requires complex manufacturing processes and intensive preconditioning regimens, such as lymphodepletion or mobilization for cell collection (*44*). In addition, challenges related to cell exhaustion and suboptimal functional activity further limit scalability, accessibility, and clinical translation (*45*). To overcome these challenges, in vivo programming of immune cells using LNP-based RNA delivery has been proposed as an alternative approach for cancer treatment. The spleen serves as the reservoir of immune cells, making it an attractive site for drug targeting. Nevertheless, efforts to develop spleen-targeting LNPs, such as modifying lipid compositions or incorporating targeting ligands, have yielded mixed results. For example, Wang *et al.* used negatively charged lipids to achieve spleen targeting, but this reduced LNP stability and mRNA expression efficiency (*13*). Rurik *et al.* used CD5-targeting antibodies to induce antifibrotic CAR T cells in mice, but these LNPs still primarily accumulated in the liver (*46*). In addition, it remains unclear which specific immune cells in the spleen are targeted by these approaches. Although Kranz *et al.* optimized net charges in mRNA-lipoplexes to target splenic DCs, most of the particles were taken up by RPMs, which have low translation efficiency (*47*). The safety and functional roles of spleen-targeted LNPs in clinical settings remain underexplored (*48*), highlighting the need for more precise delivery systems.

On the other hand, erythrocytes naturally home to the spleen and maintain close interactions with immune cells in splenic microenvironments, making them ideal cellular vehicles for immune modulation within the spleen. Although previous studies attempted to noncovalently attach nanoparticles to erythrocytes for therapeutic molecule delivery, these methods suffered from low drug payloads and rapid dissociation of nanoparticles from erythrocytes within hours postadministration (*21*). In contrast, our erythrocyte-based mRNA delivery system achieved high mRNA payloads with stable nanoparticle conjugation, enabling efficient and precise delivery to splenic immune cells. This in vivo CAR myeloid programming approach eliminates the need for lymphodepletion or other preconditioning treatments, making it more scalable, efficient, and clinically accessible than current ex vivo CAR cell therapies. Moreover, our findings suggest that in vivo–generated CAR myeloid cells act not only as direct cytotoxic effectors but also as potent immune amplifiers. By adopting a proinflammatory, antigen-presenting phenotype, they drive secondary activation of lymphocytes. This feed-forward interaction between CAR myeloid cells and adaptive immune populations sustains immune activation and may underlie long-term tumor control.

The process of erythrocyte surveillance and clearance by splenic immune cells is a well-established biological mechanism (*11*). Our findings revealed that mRNA-LNP-Ery selectively targets splenic $CD11b^+$ myeloid cells, which are critical for mediating antitumor responses. Although the exact reason for the preferential targeting of $CD11b^+$ myeloid cells remains unclear, this observation underscores the potential to refine cell-specific targeting by engineering erythrocyte membrane components. Leveraging the natural compatibility of erythrocytes with membrane modifications, future strategies can further enhance the precision of immune cell targeting. Mechanistically, erythrocyte-mediated mRNA delivery differs fundamentally from that of conventional LNPs. Whereas LNPs rely on receptor-mediated endocytosis and are frequently sequestered within endosomes, erythrocytes are internalized by myeloid cells through actin-dependent phagocytosis. Inhibition of this pathway markedly reduced erythrocyte-mediated uptake, confirming its essential role. Time-resolved confocal imaging further revealed that the mRNA cargo is internalized together with erythrocytes and that a substantial fraction of the mRNA dissociates and escapes into the cytosol before phagolysosomal fusion. This early cytosolic release markedly enhances mRNA translation efficiency. This behavior is consistent with the distinct structural and dynamic properties of phagosomes, which exhibit slower acidification kinetics and permissive membrane remodeling that allow transient cytosolic communication and facilitate ionizable lipid–mediated mRNA escape (*49*–*51*). Such delayed fusion is consistent with prior reports that phagosomes containing senescent erythrocytes exhibit incomplete acidification and limited proteolysis (*52*, *53*). Unlike rapidly acidifying endosomes, phagosomes have larger luminal volumes and slower maturation kinetics, which delay acidification and allow transient membrane remodeling events that can promote cytosolic communication. Such dynamics, together with the fusogenic properties of ionizable lipids (*54*, *55*), likely facilitate mRNA release from phagosomes before full lysosomal fusion, explaining the efficient translation observed with erythrocyte-mediated phagocytic delivery. This phagocytic uptake route offers distinct advantages over endocytosis: Phagosomes containing erythrocyte-conjugated materials often avoid lysosomal fusion, allowing the delivered mRNA to remain intact and functional. In contrast, conventional LNPs experience extensive endosomal trapping that limits cytosolic availability and therapeutic output. By overcoming these intrinsic barriers, erythrocyte-based mRNA delivery provides a highly efficient and targeted mechanism for in vivo immune-cell programming.

Despite these advances, several limitations of this study should be acknowledged. The current findings are primarily based on murine

models, and additional evaluation in experimental systems that more closely reflect human physiology will be important to further establish translational relevance. In particular, it remains to be determined whether the splenic targeting behavior, tissue biodistribution, and pharmacokinetic properties of mRNA-LNP-Ery observed in mice are conserved across species under human-relevant physiological conditions. In addition, the therapeutic scope of this study is limited to CAR constructs targeting HER2 and CD19. Although these models demonstrate the feasibility of erythrocyte-mediated in vivo generation of CAR myeloid cells, future studies will be required to assess the generalizability of this platform across a broader range of tumor antigens and disease contexts. Last, because CAR expression driven by mRNA delivery is inherently transient, the optimal dosing frequency, durability of immune reprogramming, and potential consequences of repeated administration remain to be defined. These factors will be important considerations for clinical translation and therapeutic regimen design. In conclusion, this platform leverages the unique biology of erythrocytes to enable precise, high-efficiency mRNA transfer to immune cells, representing a versatile and clinically translatable approach for advancing cancer immunotherapy and immune modulation.

MATERIALS AND METHODS

Study design

The overall objective of this study was to develop an erythrocyte-mediated mRNA delivery system (mRNA-LNP-Ery) and to evaluate its pharmacokinetic behavior, biodistribution, delivery mechanism, and therapeutic potential in cancer models. Using reporter mRNAs encoding luciferase or Cre recombinase, we assessed the biodistribution of mRNA-LNP-Ery across organs and immune cell populations in mouse models using in vivo bioluminescence imaging and flow cytometry. The cellular uptake and intracellular trafficking of mRNA-LNP-Ery were investigated using complementary in vitro assays and in vivo approaches, including confocal imaging, phagocytosis assays, and studies conducted in both WT and $Ldlr^{-/-}$ mice. The therapeutic relevance of this platform was evaluated through in vivo delivery of CAR-encoding mRNAs targeting HER2 or CD19, followed by assessment of antitumor efficacy and safety in syngeneic MC38-hHER2 and B16-hCD19 tumor models. Immune remodeling effects were further characterized by scRNA-seq, flow cytometry, and immunohistochemistry.

For in vitro experiments, at least two independent biological replicates were performed for each condition. Samples with identical pretreatment conditions were randomly assigned to experimental groups. For in vivo studies, sample sizes were determined on the basis of prior experience with comparable experimental systems and anticipated biological variability; exact animal numbers and replicate information are provided in the corresponding figure legends. Age- and sex-matched mice were used throughout, and animals were randomly allocated to treatment groups before administration. No formal blinding was implemented for in vivo experiments because of logistical constraints related to animal handling and cage identification; however, objective quantitative end points were applied wherever feasible. All animal procedures were approved by the Committee for Animal Research of Westlake University (protocols 20-043-GXF and GXF-24-134) and complied with the Guide for the Care and Use of Laboratory Animals. Data collection was continued until the predefined experimental end points were reached, as specified in the experimental protocols, with no interim stopping rules applied. No data points or animals were excluded from the analyses, and no outlier removal was performed. Detailed experimental procedures and statistical methods are provided in the figure legends and in the "Materials and Methods" section in the Supplementary Materials.

Statistical analysis

Experimental data are presented as means ± SEM unless noted otherwise. Data were analyzed by unpaired *t* test or one- and two-way analysis of variance (ANOVA) using GraphPad Prism 7.0 software, and by chi-square test or Wilcoxon rank-sum test using R (v.4.2.1 and later versions). Statistical significance is indicated as follows: ns, not significant; $*P < 0.05$; $**P < 0.01$; $***P < 0.001$. All individual level data for $n < 20$ are presented in data file S1.

Supplementary Materials

The PDF file includes:

Materials and Methods
Figs. S1 to S12
Table S1
References (*56*–*65*)

Other Supplementary Material for this manuscript includes the following:

Data file S1
MDAR Reproducibility Checklist

REFERENCES AND NOTES

1. M. Klichinsky, M. Ruella, O. Shestova, X. M. Lu, A. Best, M. Zeeman, M. Schmierer, K. Gabrusiewicz, N. R. Anderson, N. E. Petty, K. D. Cummins, F. Shen, X. Shan, K. Veliz, K. Blouch, Y. Yashiro-Ohtani, S. S. Kenderian, M. Y. Kim, R. S. O'Connor, S. R. Wallace, M. S. Kozlowski, D. M. Marchione, M. Shestov, B. A. Garcia, C. H. June, S. Gill, Human chimeric antigen receptor macrophages for cancer immunotherapy. *Nat. Biotechnol.* **38**, 947–953 (2020).
2. S. Pierini, R. Gabbasov, M. C. Oliveira-Nunes, R. Qureshi, A. Worth, S. Huang, K. Nagar, C. Griffin, L. Lian, Y. Yashiro-Ohtani, K. Ross, C. Sloas, M. Ball, B. Schott, P. Sonawane, L. Cornell, D. Blumenthal, S. Chhum, N. Minutolo, K. Ciccaglione, L. Shaw, I. Zentner, H. Levitsky, O. Shestova, S. Gill, B. Varghese, D. Cushing, S. Ceeraz DeLong, S. Abramson, T. Condamine, M. Klichinsky, Chimeric antigen receptor macrophages (CAR-M) sensitize HER2^{+} solid tumors to PD1 blockade in pre-clinical models. *Nat. Commun.* **16**, 706 (2025).
3. K. A. Reiss, M. G. Angelos, E. C. Dees, Y. Yuan, N. T. Ueno, P. R. Pohlmann, M. L. Johnson, J. Chao, O. Shestova, J. S. Serody, M. Schmierer, M. Kremp, M. Ball, R. Qureshi, B. H. Schott, P. Sonawane, S. C. DeLong, M. Christiano, R. F. Swaby, S. Abramson, K. Locke, D. Barton, E. Kennedy, S. Gill, D. Cushing, M. Klichinsky, T. Condamine, Y. Abdou, CAR-macrophage therapy for HER2-overexpressing advanced solid tumors: A phase 1 trial. *Nat. Med.* **31**, 1171–1182 (2025).
4. F. P. Polack, S. J. Thomas, N. Kitchin, J. Absalon, A. Gurtman, S. Lockhart, J. L. Perez, G. Pérez Marc, E. D. Moreira, C. Zerbini, R. Bailey, K. A. Swanson, S. Roychoudhury, K. Koury, P. Li, W. V. Kalina, D. Cooper, R. W. Frenck Jr., L. L. Hammitt, Ö. Türeci, H. Nell, A. Schaefer, S. Ünal, D. B. Tresnan, S. Mather, P. R. Dormitzer, U. Şahin, K. U. Jansen, W. C. Gruber, C4591001 Clinical Trial Group, Safety and efficacy of the BNT162b2 mRNA Covid-19 vaccine. *N. Engl. J. Med.* **383**, 2603–2615 (2020).
5. L. R. Baden, H. M. el Sahly, B. Essink, K. Kotloff, S. Frey, R. Novak, D. Diemert, S. A. Spector, N. Rouphael, C. B. Creech, J. McGettigan, S. Khetan, N. Segall, J. Solis, A. Brosz, C. Fierro, H. Schwartz, K. Neuzil, L. Corey, P. Gilbert, H. Janes, D. Follmann, M. Marovich, J. Mascola, L. Polakowski, J. Ledgerwood, B. S. Graham, H. Bennett, R. Pajon, C. Knightly, B. Leav, W. Deng, H. Zhou, S. Han, M. Ivarsson, J. Miller, T. Zaks, COVE Study Group, Efficacy and safety of the mRNA-1273 SARS-CoV-2 vaccine. *N. Engl. J. Med.* **384**, 403–416 (2021).
6. E. Rohner, R. Yang, K. S. Foo, A. Goedel, K. R. Chien, Unlocking the promise of mRNA therapeutics. *Nat. Biotechnol.* **40**, 1586–1600 (2022).
7. F. Sebastiani, M. Yanez Arteta, M. Lerche, L. Porcar, C. Lang, R. A. Bragg, C. S. Elmore, V. R. Krishnamurthy, R. A. Russell, T. Darwish, H. Pichler, S. Waldie, M. Moulin, M. Haertlein, V. T. Forsyth, L. Lindfors, M. Cárdenas, Apolipoprotein E binding drives structural and compositional rearrangement of mRNA-containing lipid nanoparticles. *ACS Nano* **15**, 6709–6722 (2021).
8. E. Blanco, H. Shen, M. Ferrari, Principles of nanoparticle design for overcoming biological barriers to drug delivery. *Nat. Biotechnol.* **33**, 941–951 (2015).

9. J. Gilleron, W. Querbes, A. Zeigerer, A. Borodovsky, G. Marsico, U. Schubert, K. Manygoats, S. Seifert, C. Andree, M. Stöter, H. Epstein-Barash, L. Zhang, V. Koteliansky, K. Fitzgerald, E. Fava, M. Bickle, Y. Kalaidzidis, A. Akinc, M. Maier, M. Zerial, Image-based analysis of lipid nanoparticle–mediated siRNA delivery, intracellular trafficking and endosomal escape. *Nat. Biotechnol.* **31**, 638–646 (2013).
10. S. M. Moghimi, D. Simberg, Pro-inflammatory concerns with lipid nanoparticles. *Mol. Ther.* **30**, 2109–2110 (2022).
11. V. Bronte, M. J. Pittet, The spleen in local and systemic regulation of immunity. *Immunity* **39**, 806–818 (2013).
12. J. Steenbrugge, E. A. De Jaeghere, E. Meyer, H. Denys, O. De Wever, Splenic hematopoietic and stromal cells in cancer progression. *Cancer Res.* **81**, 27–34 (2021).
13. X. Wang, S. Liu, Y. Sun, X. Yu, S. M. Lee, Q. Cheng, T. Wei, J. Gong, J. Robinson, D. Zhang, X. Lian, P. Basak, D. J. Siegwart, Preparation of selective organ-targeting (SORT) lipid nanoparticles (LNPs) using multiple technical methods for tissue-specific mRNA delivery. *Nat. Protoc.* **18**, 265–291 (2023).
14. Z. Huang, K. Sun, Z. Luo, J. Zhang, H. Zhou, H. Yin, Z. Liang, J. You, Spleen-targeted delivery systems and strategies for spleen-related diseases. *J. Control. Release* **370**, 773–797 (2024).
15. R. E. Mebius, G. Kraal, Structure and function of the spleen. *Nat. Rev. Immunol.* **5**, 606–616 (2005).
16. K. M. Tsoi, S. A. MacParland, X. Z. Ma, V. N. Spetzler, J. Echeverri, B. Ouyang, S. M. Fadel, E. A. Sykes, N. Goldaracena, J. M. Kaths, J. B. Conneely, B. A. Alman, M. Selzner, M. A. Ostrowski, O. A. Adeyi, A. Zilman, I. D. McGilvray, W. C. W. Chan, Mechanism of hard-nanomaterial clearance by the liver. *Nat. Mater.* **15**, 1212–1221 (2016).
17. I. V. Pivkin, Z. Peng, G. E. Karniadakis, P. A. Buffet, M. Dao, S. Suresh, Biomechanics of red blood cells in human spleen and consequences for physiology and disease. *Proc. Natl. Acad. Sci. U.S.A.* **113**, 7804–7809 (2016).
18. M. Dao, I. MacDonald, R. J. Asaro, Erythrocyte flow through the interendothelial slits of the splenic venous sinus. *Biomech. Model. Mechanobiol.* **20**, 2227–2245 (2021).
19. Y. Huang, X. Nie, X. Liu, Y. Liu, H. Yu, X. Gao, Development of a highly-efficient erythrocyte-drug covalent conjugation platform and its use in treating thrombotic disorders. *Cell Res.* **33**, 887–890 (2023).
20. Y. Liu, X. Nie, X. Yao, H. Shou, Y. Yuan, Y. Ge, X. Tong, H. Y. Lee, X. Gao, Developing an erythrocyte–MHC-I conjugate for cancer treatment. *Cell Discov.* **10**, 99 (2024).
21. Z. Zhao, A. Ukidve, V. Krishnan, A. Fehnel, D. C. Pan, Y. Gao, J. Kim, M. A. Evans, A. Mandal, J. Guo, V. R. Muzykantov, S. Mitragotri, Systemic tumour suppression via the preferential accumulation of erythrocyte-anchored chemokine-encapsulating nanoparticles in lung metastases. *Nat. Biomed. Eng.* **5**, 441–454 (2021).
22. A. Akinc, M. A. Maier, M. Manoharan, K. Fitzgerald, M. Jayaraman, S. Barros, S. Ansell, X. du, M. J. Hope, T. D. Madden, B. L. Mui, S. C. Semple, Y. K. Tam, M. Ciufolini, D. Witzigmann, J. A. Kulkarni, R. van der Meel, P. R. Cullis, The Onpattro story and the clinical translation of nanomedicines containing nucleic acid-based drugs. *Nat. Nanotechnol.* **14**, 1084–1087 (2019).
23. K. Karikó, M. Buckstein, H. Ni, D. Weissman, Suppression of RNA recognition by Toll-like receptors: The impact of nucleoside modification and the evolutionary origin of RNA. *Immunity* **23**, 165–175 (2005).
24. M. E. Ackerman, B. Moldt, R. T. Wyatt, A. S. Dugast, E. McAndrew, S. Tsoukas, S. Jost, C. T. Berger, G. Sciaranghella, Q. Liu, D. J. Irvine, D. R. Burton, G. Alter, A robust, high-throughput assay to determine the phagocytic activity of clinical antibody samples. *J. Immunol. Methods* **366**, 8–19 (2011).
25. M. Magnani, L. Rossi, V. Stocchi, L. Cucchiarini, G. Piacentini, G. Fornaini, Effect of age on some properties of mice erythrocytes. *Mech. Ageing Dev.* **42**, 37–47 (1988).
26. S. M. Lewis, A. Williams, S. C. Eisenbarth, Structure and function of the immune system in the spleen. *Sci. Immunol.* **4**, eaau6085 (2019).
27. Y. N. Zhang, W. Poon, A. J. Tavares, I. D. McGilvray, W. C. W. Chan, Nanoparticle-liver interactions: Cellular uptake and hepatobiliary elimination. *J. Control. Release* **240**, 332–348 (2016).
28. D. Bratosin, J. Mazurier, J. P. Tissier, J. Estaquier, J. J. Huart, J. C. Ameisen, D. Aminoff, J. Montreuil, Cellular and molecular mechanisms of senescent erythrocyte phagocytosis by macrophages. A review. *Biochimie* **80**, 173–195 (1998).
29. S. Shin, P. Lee, J. Han, S. N. Kim, J. Lim, D. H. Park, T. Paik, J. Min, C. G. Park, W. Park, Nanoparticle-based chimeric antigen receptor therapy for cancer immunotherapy. *Tissue Eng. Regener. Med.* **20**, 371–387 (2023).
30. G. Delidakis, J. E. Kim, K. George, G. Georgiou, Improving antibody therapeutics by manipulating the Fc domain: Immunological and structural considerations. *Annu. Rev. Biomed. Eng.* **24**, 249–274 (2022).
31. D. Schlam, R. D. Bagshaw, S. A. Freeman, R. F. Collins, T. Pawson, G. D. Fairn, S. Grinstein, Phosphoinositide 3-kinase enables phagocytosis of large particles by terminating actin assembly through Rac/Cdc42 GTPase-activating proteins. *Nat. Commun.* **6**, 8623 (2015).
32. F. K. Swirski, M. Nahrendorf, M. Etzrodt, M. Wildgruber, V. Cortez-Retamozo, P. Panizzi, J. L. Figueiredo, R. H. Kohler, A. Chudnovskiy, P. Waterman, E. Aikawa, T. R. Mempel, P. Libby, R. Weissleder, M. J. Pittet, Identification of splenic reservoir monocytes and their deployment to inflammatory sites. *Science* **325**, 612–616 (2009).
33. Q.-Q. Zhang, X. W. Hu, Y. L. Liu, Z. J. Ye, Y. H. Gui, D. L. Zhou, C. L. Qi, X. D. He, H. Wang, L. J. Wang, CD11b deficiency suppresses intestinal tumor growth by reducing myeloid cell recruitment. *Sci. Rep.* **5**, 15948 (2015).
34. L. Gabitova, B. Menchel, R. Gabbasov, S. Pierini, A. Best, K. Ross, Y. Ohtani, D. Blumenthal, S. Abramson, T. Condamine, M. Klichinsky, Abstract 1530: Anti-HER2 CAR monocytes demonstrate targeted anti-tumor activity and enable a single day cell manufacturing process. *Cancer Res.* **81**, 1530–1530 (2021).
35. M. A. Morrissey, A. P. Williamson, A. M. Steinbach, E. W. Roberts, N. Kern, M. B. Headley, R. D. Vale, Chimeric antigen receptors that trigger phagocytosis. *eLife* **7**, e36688 (2018).
36. C. Liao, K. S. Prabhu, R. F. Paulson, Monocyte-derived macrophages expand the murine stress erythropoietic niche during the recovery from anemia. *Blood* **132**, 2580–2593 (2018).
37. L. Jerby-Arnon, P. Shah, M. S. Cuoco, C. Rodman, M. J. Su, J. C. Melms, R. Leeson, A. Kanodia, S. Mei, J. R. Lin, S. Wang, B. Rabasha, D. Liu, G. Zhang, C. Margolais, O. Ashenberg, P. A. Ott, E. I. Buchbinder, R. Haq, F. S. Hodi, G. M. Boland, R. J. Sullivan, D. T. Frederick, B. Miao, T. Moll, K. T. Flaherty, M. Herlyn, R. W. Jenkins, R. Thummalapalli, M. S. Kowalczyk, I. Cañadas, B. Schilling, A. N. R. Cartwright, A. M. Luoma, S. Malu, P. Hwu, C. Bernatchez, M. A. Forget, D. A. Barbie, A. K. Shalek, I. Tirosh, P. K. Sorger, K. Wucherpfennig, E. M. van Allen, D. Schadendorf, B. E. Johnson, A. Rotem, O. Rozenblatt-Rosen, L. A. Garraway, C. H. Yoon, B. Izar, A. Regev, A cancer cell program promotes T cell exclusion and resistance to checkpoint blockade. *Cell* **175**, 984–997.e24 (2018).
38. X. Zhou, Y. Wang, Z. Dou, G. Delfanti, O. Tsahouridis, C. M. Pellegry, M. Zingarelli, G. Atassi, M. G. Woodcock, G. Casorati, P. Dellabona, W. Y. Kim, L. Guo, B. Savoldo, A. Tsagaratou, J. J. Milner, L. S. Metelitsa, G. Dotti, CAR-redirected natural killer T cells demonstrate superior antitumor activity to CAR-T cells through multimodal CD1d-dependent mechanisms. *Nat. Cancer* **5**, 1607–1621 (2024).
39. S. R. Gordon, R. L. Maute, B. W. Dulken, G. Hutter, B. M. George, M. N. McCracken, R. Gupta, J. M. Tsai, R. Sinha, D. Corey, A. M. Ring, A. J. Connolly, I. L. Weissman, PD-1 expression by tumour-associated macrophages inhibits phagocytosis and tumour immunity. *Nature* **545**, 495–499 (2017).
40. D. Stahl, P. Gödel, H. Balke-Want, R. Gholamipoorfard, P. Segbers, L. Tetenborg, M. Koker, J. Dörr, L. Gregor, D. Bachurski, F. Rose, A. G. Simon, Z. Good, J. Jakob, B. Häupl, M. Nill, R. Flümann, T. Riet, D. Lange, S. J. Blakemore, H. Baurmann, C. A. Voltin, N. Potter, L. Schlözer, M. Freihammer, S. Wagener-Ryczek, A. I. Iuga, J. M. Heger, H. Ludwig, J. K. Schleifenbaum, J. Propp, P. J. Bröckelmann, R. D. Jachimowicz, G. Knittel, S. Borchmann, S. Merkelbach-Bruse, C. Pallasch, M. Peifer, J. Rybniker, A. Quaas, M. Nitz, J. Brägelmann, W. Müller, T. Persigehl, K. Bozek, S. J. Theobald, R. Büttner, T. Oellerich, M. Hallek, S. Kobold, M. Chmielewski, H. C. Reinhardt, C. Mackall, N. Abedpour, P. Borchmann, R. T. Ullrich, CSF1R^{+} myeloid-monocytic cells drive CAR-T cell resistance in aggressive B cell lymphoma. *Cancer Cell* **43**, 1476–1494.e10 (2025).
41. I. Albino Rat, S. H. Webster, E. J. Liljegren, D. J. Zimmer, Organ: Body weight ratios for liver, kidneys and spleen of laboratory animals. *J. Anat.* **81**, 477–513 (1947).
42. J. Zak, I. Pratumchai, B. S. Marro, K. L. Marquardt, R. B. Zavareh, L. L. Lairson, M. B. A. Oldstone, J. A. Varner, L. Hegerova, Q. Cao, U. Farooq, V. P. Kenkre, V. Bachanova, J. R. Teijaro, JAK inhibition enhances checkpoint blockade immunotherapy in patients with Hodgkin lymphoma. *Science* **384**, eade8520 (2024).
43. D. M. Calcagno, R. P. Ng Jr., A. Toomu, C. Zhang, K. Huang, A. D. Aguirre, R. Weissleder, L. B. Daniels, Z. Fu, K. R. King, The myeloid type I interferon response to myocardial infarction begins in bone marrow and is regulated by Nrf2-activated macrophages. *Sci. Immunol.* **5**, eaaz1974 (2020).
44. Y. Abdou, P. R. Pohlmann, R. T. Maziarz, H. S. Murthy, Y. Yuan, A. Krishnamurthy, K. A. Reiss, J. Isaacs, D. Blumenthal, L. Gabitova, B. Menchel, K. Locke, J. Wetzel, M. Klichinsky, D. Cushing, T. Condamine, D. Sohal, A phase 1, first-in-human study of autologous monocytes engineered to express an anti-HER2 chimeric antigen receptor (CAR) in participants with HER2-overexpressing solid tumors. *J. Clin. Oncol.* **42**, TPS2682 (2024).
45. A. Mullard, In vivo CAR T cells move into clinical trials. *Nat. Rev. Drug Discov.* **23**, 727–730 (2024).
46. J. G. Rurik, I. Tombácz, A. Yadegari, P. O. Méndez Fernández, S. V. Shewale, L. Li, T. Kimura, O. Y. Soliman, T. E. Papp, Y. K. Tam, B. L. Mui, S. M. Albelda, E. Puré, C. H. June, H. Aghajanian, D. Weissman, H. Parhiz, J. A. Epstein, CAR T cells produced in vivo to treat cardiac injury. *Science* **375**, 91–96 (2022).
47. L. M. Kranz, M. Diken, H. Haas, S. Kreiter, C. Loquai, K. C. Reuter, M. Meng, D. Fritz, F. Vascotto, H. Hefesha, C. Grunwitz, M. Vormehr, Y. Hüsemann, A. Selmi, A. N. Kuhn, J. Buck, E. Derhovanessian, R. Rae, S. Attig, J. Diekmann, R. A. Jabulowsky, S. Heesch, J. Hassel, P. Langguth, S. Grabbe, C. Huber, Ö. Türeci, U. Sahin, Systemic RNA delivery to dendritic cells exploits antiviral defence for cancer immunotherapy. *Nature* **534**, 396–401 (2016).
48. S. Nie, B. Yang, R. Ma, L. Zha, Y. Qin, L. Ou, X. Chen, L. Li, Synthetic nanomaterials for spleen-specific mRNA delivery. *Biomaterials* **314**, 122859 (2025).

49. G. D. Fairn, S. Grinstein, How nascent phagosomes mature to become phagolysosomes. *Trends Immunol.* **33**, 397–405 (2012).
50. R. M. Yates, D. G. Russell, Phagosome maturation proceeds independently of stimulation of toll-like receptors 2 and 4. *Immunity* **23**, 409–417 (2005).
51. M. Desjardins, Biogenesis of phagolysosomes: The 'kiss and run' hypothesis. *Trends Cell Biol.* **5**, 183–186 (1995).
52. M. V. Baranov, M. Kumar, S. Sacanna, S. Thutupalli, G. van den Bogaart, Modulation of immune responses by particle size and shape. *Front. Immunol.* **11**, 607945 (2020).
53. D. Paul, S. Achouri, Y. Z. Yoon, J. Herre, C. E. Bryant, P. Cicuta, Phagocytosis dynamics depends on target shape. *Biophys. J.* **105**, 1143–1150 (2013).
54. S. Sabnis, E. S. Kumarasinghe, T. Salerno, C. Mihai, T. Ketova, J. J. Senn, A. Lynn, A. Bulychev, I. McFadyen, J. Chan, Ö. Almarsson, M. G. Stanton, K. E. Benenato, A novel amino lipid series for mRNA delivery: Improved endosomal escape and sustained pharmacology and safety in non-human primates. *Mol. Ther.* **26**, 1509–1519 (2018).
55. M. Maugeri, M. Nawaz, A. Papadimitriou, A. Angerfors, A. Camponeschi, M. Na, M. Hölttä, P. Skantze, S. Johansson, M. Sundqvist, J. Lindquist, T. Kjellman, I. L. Mårtensson, T. Jin, P. Sunnerhagen, S. Östman, L. Lindfors, H. Valadi, Linkage between endosomal escape of LNP-mRNA and loading into EVs for transport to other cells. *Nat. Commun.* **10**, 4333 (2019).
56. M. Yanez Arteta, T. Kjellman, S. Bartesaghi, S. Wallin, X. Wu, A. J. Kvist, A. Dabkowska, N. Székely, A. Radulescu, J. Bergenholtz, L. Lindfors, Successful reprogramming of cellular protein production through mRNA delivered by functionalized lipid nanoparticles. *Proc. Natl. Acad. Sci. U.S.A.* **115**, E3351–E3360 (2018).
57. G. T. Hermanson, in *Bioconjugate Techniques (Third Edition)*, G. T. Hermanson, Ed. (Academic Press, 2013), pp. 229–258.
58. A. M. van Cromvoirt, S. Fenk, A. Sadafi, E. V. Melnikova, D. A. Lagutkin, K. Dey, I. Y. Petrushanko, I. Hegemann, J. S. Goede, A. Bogdanova, Donor age and red cell age contribute to the variance in lorrca indices in healthy donors for next generation ektacytometry: A pilot study. *Front. Physiol.* **12**, 639722 (2021).
59. J. Yang, M. Kubera, A. Zelek-Molik, I. Nalepa, V. Hukkanen, P. J. Lindsberg, S. Meri, R. Seljelid, Splenectomy and adoptive cell transfer reveal a prominent role for splenic memory lymphocytes in the development of chronic relapsing experimental autoimmune encephalomyelitis. *Scand. J. Immunol.* **52**, 356–361 (2000).
60. J. C. Gigliotti, L. Huang, A. Bajwa, H. Ye, E. H. Mace, J. A. Hossack, K. Kalantari, T. Inoue, D. L. Rosin, M. D. Okusa, Ultrasound modulates the splenic neuroimmune axis in attenuating AKI. *J. Am. Soc. Nephrol.* **26**, 2470–2481 (2015).
61. H. Wong, E. F. Choo, B. Alicke, X. Ding, H. la, E. McNamara, F. P. Theil, J. Tibbitts, L. S. Friedman, C. E. C. A. Hop, S. E. Gould, Antitumor activity of targeted and cytotoxic agents in murine subcutaneous tumor models correlates with clinical response. *Clin. Cancer Res.* **18**, 3846–3855 (2012).
62. D. J. Schofield, J. Percival-Alwyn, M. Rytelewski, J. Hood, R. Rothstein, L. Wetzel, K. McGlinchey, G. Adjei, A. Watkins, L. A. Machiesky, W. Chen, J. Andrews, M. Groves, M. Morrow, R. A. Stewart, A. Leinster, R. W. Wilkinson, S. A. Hammond, N. Luheshi, C. Dobson, M. Oberst, Activity of murine surrogate antibodies for durvalumab and tremelimumab lacking effector function and the ability to deplete regulatory T cells in mouse models of cancer. *MAbs* **13**, 1857100 (2021).
63. G. X. Y. Zheng, J. M. Terry, P. Belgrader, P. Ryvkin, Z. W. Bent, R. Wilson, S. B. Ziraldo, T. D. Wheeler, G. P. McDermott, J. Zhu, M. T. Gregory, J. Shuga, L. Montesclaros, J. G. Underwood, D. A. Masquelier, S. Y. Nishimura, M. Schnall-Levin, P. W. Wyatt, C. M. Hindson, R. Bharadwaj, A. Wong, K. D. Ness, L. W. Beppu, H. J. Deeg, C. McFarland, K. R. Loeb, W. J. Valente, N. G. Ericson, E. A. Stevens, J. P. Radich, T. S. Mikkelsen, B. J. Hindson, J. H. Bielas, Massively parallel digital transcriptional profiling of single cells. *Nat. Commun.* **8**, 14049 (2017).
64. A. Butler, P. Hoffman, P. Smibert, E. Papalexi, R. Satija, Integrating single-cell transcriptomic data across different conditions, technologies, and species. *Nat. Biotechnol.* **36**, 411–420 (2018).
65. G. Yu, L. G. Wang, Y. Han, Q. Y. He, clusterProfiler: An R package for comparing biological themes among gene clusters. *Omics* **16**, 284–287 (2012).

Acknowledgments: We appreciate the technical support from the Biomedical Research Core Facilities, Laboratory Animal Resources Center, and High-Performance Computing Center of Westlake University. We thank Y. Feng and J. Sun for the experimental guidance and for providing cell lines. **Funding:** This work was supported by the Key R&D Program of Zhejiang Province (grants 2024C03170 and 2024C03089 to X.G.) and the National Key R&D Program of China (grants 2022YFA1103300 and 2024YFA1106900 to H.-Y.L.). **Author contributions:** Conceptualization: X.G. Methodology: X.N., Y.L., Y.S., X.Y., Y.C., H.-Y.L., and X.G. Validation: X.N., Y.L., Y.S., X.Y., Y.C., H.-Y.L., and X.G. Formal analysis: X.N., Y.L., X.Y., and X.G. Investigation: X.N., Y.L., Y.S., X.Y, and X.G. Resources: H.-Y.L. and X.G. Data curation: X.N., Y.L., Y.S., X.Y, Y.C., and X.G. Writing—original draft: X.N., Y.L., and X.G. Writing—review and editing: X.N., Y.L., X.Y., H.-Y.L., and X.G. Visualization: X.N., Y.L., Y.S., X.Y., and X.G. Project administration: X.N. and X.G. Supervision: X.G. Funding acquisition: H.-Y.L. and X.G. **Competing interests:** X.G. is a founder of Westlake Therapeutics Co., Ltd. and a member of its scientific advisory board. X.G., X.N., and Y.S. are inventors on patent applications (Novel RBC-Based Delivery System for Nucleic Acids, PCT/CN2025/116712) submitted by Westlake University and Westlake Therapeutics Co., Ltd. The other authors declare that they have no competing interests. **Data, code, and materials availability:** All data associated with this study are present in the paper or the Supplementary Materials. The data described in this manuscript have been deposited in the Genome Sequence Archive (GSA) at the National Genomics Data Center under accession number CRA033093 and are publicly available at https://ngdc.cncb.ac.cn/gsa/browse/CRA033093. The analysis code is available and was implemented using previously published tools, as detailed in Materials and Methods. The R scripts for analysis and visualization have been archived in Zenodo (https://zenodo.org/records/17567656). All materials used or generated in this study are commercially available or will be supplied upon reasonable request.

Submitted 30 April 2025
Resubmitted 11 November 2025
Accepted 4 March 2026
Published 25 March 2026
10.1126/scitranslmed.ady6730

Science Translational Medicine

In vivo generation of CAR myeloid cells through erythrocyte-mediated mRNA delivery for cancer immunotherapy

Xiaoqian Nie, Yuehua Liu, Yuting Song, Xingyun Yao, Yangyang Chen, Hsiang-Ying Lee, and Xiaofei Gao

Sci. Transl. Med. **18** (842), eady6730. DOI: 10.1126/scitranslmed.ady6730

Editor's summary

Chimeric antigen receptor (CAR)–modified myeloid cells have emerged as promising immunotherapy candidates in the treatment of solid tumors. Here, Nie *et al.* developed a method for the targeting of splenic myeloid cells to generate CAR-modified myeloid cells in vivo. mRNA-loaded lipid nanoparticles were conjugated to erythrocytes, which naturally home to spleens, enabling the efficient delivery of mRNA encoding CARs to myeloid cells and the subsequent generation of functional CAR myeloid cells in vivo. CAR myeloid cells targeting human epidermal growth factor receptor 2 (HER2) or CD19 reduced tumor progression and increased the infiltration of T and natural killer (NK) cells. This work provides an innovative approach for the in vivo generation of myeloid-based CAR effector cells. —Amy E. Baek

Science Translational Medicine (ISSN 1946-6242) is published by the American Association for the Advancement of Science. 1200 New York Avenue NW, Washington, DC 20005. The title *Science Translational Medicine* is a registered trademark of AAAS.